https://ntrs.nasa.gov/search.jsp?R=19770024210 2020-03-22T07:30:26+00:00Z

NASA Technical Paper 1034

Development and Verification of Real-Time, Hybrid Computer Simulation of F100-PW-100(3) Turbofan Engine

John R. Szuch, Kurt Seldner,
and David S. Cwynar

Lewis Research Center
Cleveland, Ohio

NASA
National Aeronautics
and Space Administration

Scientific and Technical Information Office

1977

CONTENTS

DEVELOPMENT AND VERIFICATION OF REAL-TIME, HYBRID COMPUTER SIMULATION OF F100-PW-100(3) TURBOFAN ENGINE

by John R. Szuch, Kurt Seldner, and David S. Cwynar

Lewis Research Center

SUMMARY

In recent years, there has been increased interest in developing digital, electronic controls for airbreathing propulsion systems. Real-time computer simulations of engines can facilitate the development of these digital controls. The engine simulation provides a "test-bed" for evaluating new control laws and for checking and "debugging" the control software prior to engine testing. This report describes a real-time, hybrid computer simulation of the Pratt & Whitney F100-PW-100(3) augmented turbofan engine. The simulation is intended to support controls research programs involving that engine. The simulation has both steady-state and transient calculation capabilities. This report describes the modifications that were made to a previously developed simulation of the F100-PW-100(1) engine in order to match the predicted performance of the more advanced F100-PW-100(3) engine. Baseline performance data were obtained from Pratt & Whitney's digital simulation of the engine. Data are presented to show that the real-time simulation does match the baseline steady-state and transient performance over a wide range of flight conditions and power settings. This report also includes the equations which describe the F100-PW-100(3) engine model, FORTRAN listings of the digital portion of the simulation, and analog patching diagrams.

INTRODUCTION

Over the past several years, aircraft operational requirements have dictated the development of gas turbine engines which deliver increased performance over a wider operating range. These development efforts have resulted in today's complex, augmented turbofan engines and will, undoubtedly, lead to increasingly complex, variable-cycle engines in the future.

It is not surprising that, as engines have become more sophisticated, the task of controlling those engines to provide safe and stable operation with increased performance has also become more difficult. As a result, there has been increased interest in applying multivariable (optimal) control theory to the engine control problem (refs. 1 to 4). These advanced control concepts, however, require the use of a digital computer with its inherent precision, logic, and memory capabilities. The digital computer provides the control system with more flexibility and versatility then is currently provided by hydromechanical controls (ref. 5).

It has been shown in references 6 to 8 that the use of real-time computer simulations of engines can facilitate the development of digital controls. The engine simulation provides a "test-bed" for evaluating new control laws and for checking and debugging of the actual control software prior to engine testing. A real-time simulation also allows the control developer to evaluate the timing and sequencing within the digital control and to predict the effects of extended digital sampling intervals (ref. 9) on engine performance. This report describes a real-time, hybrid computer simulation of the Pratt & Whitney F100-PW-100(3) augmented turbofan engine. The simulation has both steady-state and transient calculation capabilities and is intended for supporting controls research programs involving that engine. The report describes the modifications that were made to a previously developed simulation of the F100-PW-100(1) engine (ref. 7) in order to match predicted F100-PW-100(3) engine performance. Comparisons of hybrid simulation and baseline digital simulation data were made over a wide range of flight conditions and power settings. The baseline performance data were obtained from Pratt & Whitney's digital simulation of the engine. This report includes the results of the comparisons, simulation equations, FORTRAN listings, and analog patching diagrams.

ENGINE DESCRIPTION

The Pratt & Whitney F100-PW-100(3) engine (fig. 1) is an axial, mixed-flow, augmented, twin-spool, low-bypass-ratio turbofan. It features improved fan performance over the earlier F100-PW-100(1) version. A single inlet is used for both the fan airflow and the engine core airflow. Airflow leaving the fan is separated into two flow streams: one stream passing through the engine core and the other stream passing through the annular fan duct. The three-stage fan is connected by a through-shaft to the two-stage, low-pressure turbine. A ten-stage compressor is connected by a hollow shaft to the two-stage, high-pressure turbine. The fan has variable, trailing edge, inlet guide vanes. The compressor has a variable inlet guide vane followed by two variable stator vanes. Engine airflow bleed is extracted at the compressor exit and discharged through the fan duct during starting. Compressor discharge bleed air is also used to cool the high- and low-pressure turbine blades and to power the augmentor turbopump.

The main combustor consists of an annular diffuser and a chamber with 16 fuel nozzles. The engine core and fan duct streams combine in an augmentor and are discharged through a variable convergent-divergent nozzle. The augmentor consists of a diffuser section and five concentric fuel manifolds (zones).

The engine's bill-of-material (BOM) control system consists of a hydromechanical fuel control system and an electronic supervisory control system. The hydromechanical fuel control system (1) meters fuel to the main combustor as a function of the power lever angle PLA, the compressor speed N_H, the fan discharge total temperature T_{13}, and the compressor discharge static pressure $P_{s,3}$, (2) positions the compressor vanes to improve starting and high Mach number characteristics, (3) meters fuel to the five augmentor zones as a function of PLA, T_{13}, and $P_{s,3}$, and (4) controls the nozzle area so as to maintain the desired engine airflow during augmented operation. (All symbols are defined in appendix A. Numerical subscripts refer to locations in the engine (e.g., fig. 1).) The electronic supervisory control (1) positions the inlet guide vanes to improve inlet distortion tolerance and fan efficiency, (2) trims the main combustor fuel flow to satisfy engine limits, and (3) trims the nozzle area to satisfy engine airflow requirements.

ENGINE SIMULATION

Engine Model

The mathematical model which described the performance of the F100-PW-100(1) engine was patterned after Pratt & Whitney's digital simulation (CCD 1015) of that engine and was reported in reference 7. Subsequent modifications were made to elements of that model to match the performance of the F100-PW-100(3) engine as predicted by the corresponding digital simulation (CCD 1103-1.0). Those modifications are described in the following section. The basic structure of the mathematical model was not changed, however. Figure 2 contains a computational flow diagram of the F100-PW-100(3) real-time simulation. Appendix B contains a complete list of equations which define the simulation model. Table I contains a list of engine design parameters for the F100-PW-100(3) simulation.

Simulation Modifications

The equations describing the mathematical model of the F100-PW-100(3) engine were implemented on the Lewis Research Center's hybrid computing system. This system consists of an EAI model 640 digital computer, a model 680 analog computer, and a model 681 analog computer. The split of the computational load between the digital and analog computers was basically the same as that employed in the earlier F100-PW-100(1) simulation (ref. 7). The modifications that were made to the digital portion of that simulation included the following.

First, in the earlier F100-PW-100(1) simulation, all analog inputs to the digital computer were sampled at the beginning of the digital cycle, and all outputs to the analog computer were transferred after all of the digital calculations were completed. From a dynamic standpoint, this proved to be the worst approach since it resulted in the greatest effective time delay - hence, phase shift (refs. 10 to 12). In the F100-PW-100(3) simulation, the analog inputs to the digital computer are sampled as needed, and the resultant digital data are transferred to the analog computer as soon as they are available (on a component by component basis). This approach results in a significant reduction in the phase shift associated with individual computational loops (ref. 12) since the calculation time for each loop is much less than the total update time. Auxiliary calculations such as the calculation of engine thrust and surge margins contribute only the total update time.

Second, the fan and compressor performance maps represented by equations (B1), (B2), and (B15) were based on axial vane positions in the earlier F100-PW-100(1) simulation. This necessitated shifting the map data when operating at low corrected speeds where the vanes are cambered. To minimize this shifting in the F100-PW-100(3) simulation, the fan and compressor maps were regenerated with the vanes on their nominal schedules. Therefore, no shifting of the map data is required when the vanes are on their schedules. During transients and other off-schedule conditions the required shifting of corrected airflows is accomplished by equations (B3) and (B16) with the shifts computed from bivariate functions of corrected speed and vane position.

Third, to better match the F100-PW-100(3) baseline digital data over the entire flight envelope, an empirical Reynolds number effect on fan performance was added. A shift in the fan corrected airflow (eq. (B3)) is computed as a piecewise linear function of the Reynold's number index (eqs. (B4) and (B5)).

Fourth, all the bivariate component performance maps and shift functions were regenerated to match the predicted F100-PW-100(3) steady-state performance. Those curves are shown in figures 3 to 8.

Fifth, surge margin calculations were added for the fan (eqs. (B9) to (B12)) and the compressor (eqs. (B19) to (B22)). In each case, the critical pressure ratio was fit by a quadratic function of the corrected airflow at each of the extreme vane positions. The quadratic functions were based on fits of digital simulation data.

Sixth, the exhaust nozzle exit area A_8 was fit by a linear function (eq. (B52)) of the nozzle throat area A_7 and the nozzle inlet temperature T_7 for each of two ranges of flight Mach number. In the earlier F100-PW-100(1) simulation, the effect of nozzle heating (T_7) was not considered.

Seventh, the inlet calculations of P_2 and T_2 were eliminated in the F100-PW-100(3) simulation. These variables are transferred as input to the digital portion of the hybrid computer from the analog computer, thus allowing operation of the simulation during changes in the flight condition.

Lastly, in the earlier F100-PW-100(1) simulation, the same digital program that was used to perform the required calculations was also used for input and scaling of component performance data and for setup of the analog consoles. In the F100-PW-100(3) simulation, these functions are performed by separate digital programs. The scaled, component performance data are shared by the data input program, the main digital program, and the function generation routines through the use of COMMON blocks.

Appendix C contains a FORTRAN listing of the digital portion of the F100-PW-100(3) real-time hybrid computer simulation. Reference 6 contains a detailed discussion of the digital program structure including the MAP2 and MAP2L function generation routines.

Modifications were also made to the analog portion of the F100-PW-100(1) real-time simulation. These included the following: first, to better match the predicted F100-PW-100(3) augmentor pressure drop, the pressure drop was computed using the total augmentor gas flow (including augmentor fuel flow) and the discharge temperature T_7 (eq. (B41)). In the earlier F100-PW-100(1) simulation, the effects of augmentor fuel flow and its associated energy release were not included. Second, the augmentor efficiency and duct pressure drop curves (eqs. (B43) and (B45)) were regenerated to better match digital simulation data over the entire flight envelope. The new curves are shown in figures 9 and 10. Third, the exhaust nozzle discharge coefficient was fit by a piecewise-linear function of the nozzle pressure ratio (eq. (B49)) having more segments than in the earlier F100-PW-100(1) simulation. Fourth, in the F100-PW-100(1) simulation, the fan discharge (core side) and compressor discharge specific heats were assumed to be linear functions of the corresponding temperatures for the purpose of computing the required torques. The intercepts of the linear functions were adjusted at the military power setting to match the baseline rotor speeds at each flight condition. Changes in flight condition could not realistically be accomplished, however, because of the wide range of intercept values. To eliminate this problem in the F100-PW-100(3) simulation, the intercepts were also fit by linear functions of the fan inlet pressure and temperature (eqs. (B80) and (B85)). Only slight adjustments of the resultant intercepts were then required to match rotor speeds after changes in the flight condition. Realistic changes in the flight condition could be accomplished with fixed intercept values.

Lastly, calculations of the fan discharge $(P - P_S)/P$, for both the duct and core sides, were added to the real-time simulation (eqs. (B87) and (B88)). Figure 11 shows the functional relation between $(P - P_S)/P$ and the compressible flow parameter.

Appendix D contains the analog patching diagrams for the F100-PW-100(3) real-time, hybrid computer simulation.

Simulation Requirements

The digital portion of the F100-PW-100(3) real-time simulation consumed 12 440 words of core storage (including data). The supplemental data input program consumed 7144 words of core storage (including data). The digital computer update time, which was approximately 7.5 milliseconds, resulted in stable, real-time operation.

Both analog computers were fully utilized. For example, the full complement of 24 multipliers on the 680 analog computer and 30 multipliers on the 681 analog computer were used. In addition, the full complement of 6 digital to analog multipliers on the 680 analog computer was used. A total of 189 potentiometers was required. The eight digitally set, univariate function generators available on the 681 analog computer were also used.

RESULTS AND DISCUSSION

The usefulness of the F100-PW-100(3) real-time, hybrid computer simulation depends on its ability to accurately represent the physical engine over the desired range of operation. It should match the steady-state and the transient engine performance for power settings from idle to full augmentation (maximum thrust) at altitudes and flight speeds within the engine operating envelope. Figure 12 shows the flight conditions selected for evaluation.

Procedure

As previously stated, the basis for comparison of hybrid simulation data was the engine manufacturer's digital simulation of the engine (CCD 1103-1.0). That simulation also included a simulation of the BOM control logic. The digital simulation of the engine and control could be run in either a steady-state (fixed PLA) or transient (time-varying PLA) mode.

All of the selected flight conditions (fig. 12) were first run in the steady-state mode with PLA ranging from the minimum allowable setting to the maximum thrust setting of 130°. The minimum allowable setting (idle) was dictated by the control and was based on inlet airflow requirements and minimum combustor pressure limits. For the three subsonic conditions having altitudes lower than 10 kilometers, the idle setting was 20°. For the 13.72 km/M_n = 0.9 condition, the idle setting was 30°. For the three supersonic conditions, power settings lower than 83° were not permitted.

The steady-state data obtained from the digital simulation included (1) values for the control variables such as main combustor fuel flow and (2) values for selected engine variables such as fan speed. The hybrid computer simulation was then evaluated in steady state at each flight condition and power setting by setting the analog control inputs at the appropriate values and then recording the resulting values of the selected engine variables. In this way, the simulation could be evaluated without requiring a separate control simulation. This open-loop approach ensured that observed differences between hybrid and digital simulation data were attributable to the hybrid simulation and not to control simulation errors. The following section compares the F100-PW-100(3) hybrid simulation and baseline digital steady-state data at the selected flight conditions.

The four subsonic flight conditions (fig. 12) were also run on the digital simulation in the transient mode. In each case, the PLA was initialized as its minimum value and then stepped to 83° (at $t = 0$ sec). The 83° setting was maintained for 10 seconds at which time the PLA was stepped down to its minimum value. The transient data obtained from the digital simulation provided time histories of both the control variables and the selected engine variables. The hybrid simulation was then evaluated for transient operation by scheduling the control inputs to the hybrid simulation to match the digital time histories. The resulting engine response data were recorded and subsequently compared with the digital results. As in the steady-state evaluation, this open-loop approach eliminated the need for a separate, real-time control simulation, and it allowed the isolation of engine simulation errors. A following section (p. 9) compares the transient data obtained with the F100-PW-100(3) hybrid computer simulation with the corresponding baseline digital data.

Steady-State Simulation Results

The verification of the steady-state performance of the F100-PW-100(3) real-time simulation was accomplished by operating the simulation in an open-loop manner at each of the flight conditions shown in figure 12. At each power setting, the values of the main combustor fuel flow, exhaust nozzle area, fan inlet guide vane angle, compressor stator vane angle, and augmentor fuel flow were set to match the baseline digital values. The engine variables selected for the steady-state comparison were fan speed, compressor speed, main combustor pressure and temperature, net thrust, fan-tip pressure ratio, total fan corrected airflow, compressor pressure ratio, and compressor corrected airflow. Agreement of hybrid and baseline digital values for these variables would represent good, overall steady-state verification of the real-time simulation.

Figures 13 to 17 contain plots of the hybrid and digital steady-state data at the selected flight conditions. For convenience, the engine variables were plotted against the PLA which corresponded to the set of control variables. It should be noted that, at each flight condition, the plot scales were expanded to match the observed range of the data. The scale expansion was most significant at the supersonic flight conditions.

Prior to recording steady-state, hybrid simulation data at each flight condition, the fan and compressor discharge specific heats were adjusted to achieve a match of baseline rotor speeds at the 83° power setting as shown in figures 13 and 14. Agreement of hybrid and digital simulation data at other power settings, however, was dependent on the accuracy of the individual component models (i.e., fan, compressor, nozzle, etc.). Agreement of hybrid and digital data at these conditions would serve to substantiate the simulation simplifications that were required to achieve real-time operation.

Figure 13(a) shows excellent agreement of fan speed along the entire sea-level/static operating line. This was attributed to the fact that the temperature-sensitive specific heat relations (eqs. (B80) and (B85)) were established at the sea-level/static condition. Figures 13(b), (c), and (d) show good agreement at the other flight conditions although some discrepancies were observed in the midpower range at the higher altitudes. These errors were less than 2 to 3 percent of the design fan speed. Figures 13(e), (f), and (g) show the results of the fan speed comparison for the 6.096 km/M_n = 1.8, 12.19 km/M_n = 2.2, and 17.83 km/M_n = 2.15 conditions, respectively. For these conditions, the comparison was limited to power settings of 83° and above. For these conditions, good agreement in fan speed was also observed. The errors were generally less than 2 percent of the design speed and were attributed to the assumption of constant gas properties in the hybrid simulation model of the exhaust nozzle.

Figure 14 compares the hybrid and baseline digital results for the compressor speed. For all power settings below 83°, the observed errors were less than 3.5 percent of the design speed. For the supersonic, augmented operating points, the errors were less than 1.1 percent.

Figures 15 and 16 compare the baseline digital and hybrid simulation values for the main combustor and temperature, respectively. As in the case of the rotor speeds, excellent agreement was observed for power settings below 83° throughout the operating envelope. Errors were generally less than 3.5 percent of the design value. For the supersonic, augmented conditions, errors in the main combustor pressure and temperature were less than 2.1 percent.

Figure 17 shows the comparison of net thrust for the selected flight conditions. In the thrust calculation, a constant velocity coefficient was assumed and, as in the calculation of the exhaust nozzle flow, constant gas properties were assumed. Even with these simplifications, generally good agreement between hybrid and baseline digital values for thrust was observed. Excellent agreement was observed at the subsonic conditions. However, differences of up to 9 percent of the design maximum thrust were observed at supersonic, augmented conditions (see fig. 17(f)).

The fan and compressor operating lines are shown in figures 18 and 19, respectively. Good agreement between the baseline digital and hybrid simulation data was obtained for all flight conditions. Some discrepancy in fan corrected airflow (about 2.5 percent of the design value) was observed at the 13.72 km/M_n = 0.9 condition for high power settings. This error is attributed to Reynolds number effects, since this condition represented a lower Reynolds number index than the other selected subsonic conditions. An attempt was made to incorporate a fan airflow shift as a function of the Reynolds number index, but its adequacy was limited by a restriction on the maximum digital update time allowable for real-time operation. Good agreement was also observed for the compressor operating line. A maximum error of 4 percent in corrected airflow and 3.5 percent in pressure ratio was observed at the 3.048 km/M_n = 0.9 condition at the idle power setting.

The results presented in figures 13 to 19 indicate that the hybrid simulation adequately matches the baseline digital simulation in representing the steady-state behavior of the F100-PW-100(3) engine. The hybrid simulation errors (relative to the digital simulation) that were observed were sufficiently small so as to indicate that the hybrid simulation could be used to evaluate steady-state control functions such as speed regulation, temperature limiting, and surge protection.

Transient Simulation Results

The previous section demonstrated the capability of the F100-PW-100(3) real-time, hybrid computer simulation to predict the steady-state performance of the engine. The hybrid simulation must also predict the transient performance of the engine so as to serve as a tool for developing research control systems. The comparison between baseline digital and hybrid simulation data is presented for the four subsonic flight conditions shown in figure 12. The subsonic conditions were selected since they permitted variations in the PLA below the 83° setting.

The five control inputs to the hybrid simulation were scheduled as functions of time to match baseline digital values for a power lever ramp (slam) from the idle setting to the 83° power setting. The schedules included a power lever cutback (chop) from 83°

to idle 10 seconds after the initiation of the transient. The open-loop operation was selected for the transient evaluation to allow the isolation of simulation errors from potential control simulation errors.

Figure 20 shows the comparison of baseline digital and hybrid simulation responses to the simulated power lever movement at the sea-level/static condition. The responses of fan speed, compressor speed, compressor discharge pressure, main combustor temperature, and thrust are presented. A slightly higher fan speed overshoot (about 0.8 percent) and faster deceleration were observed for the hybrid simulation (fig. 20(a)). The hybrid simulation response of compressor speed (fig. 20(b)) was slightly faster for both acceleration and deceleration. This was attributed to the simplifications used in modeling the compressor temperature ratio (torque). Figure 20(c) shows the responses of the baseline digital and hybrid simulation values of compressor discharge pressure. The responses match quite well except for a discrepancy (about 3.5 percent) at the end of the acceleration. This error was attributed to the simplified compressor temperature ratio calculation in the hybrid simulation. Figure 20(d) compares the digital and hybrid simulation responses of the main combustor temperature. The most notable difference in the responses was that the hybrid simulation resulted in a 4 percent lower temperature rise at the start of the acceleration. This temperature difference was maintained throughout the acceleration. The hybrid simulation response exhibited no temperature overshoot while the baseline digital response overshot the final temperature by 3 percent. These differences could have been caused by any number of simplifying assumptions in the hybrid simulation. One of these was the absence of any pressure effects in the main combustor efficiency calculation. Figure 20(e) shows a similar discrepancy (about 2 percent) in the thrust responses at the end of the acceleration. The observed discontinuity in the hybrid simulation thrust was due to a simplification in the thrust calculation. Because of limits on the digital calculation time, it was not possible to accurately model the nozzle performance when normal shocks would exist in the nozzle's divergent section. Since this condition only exists at low altitude, low speed, low power conditions, it was not considered to be a serious problem. The assumption was made that flow at the nozzle throat would be either subsonic or sonic (with the shock expelled). Therefore, the discontinuity represented a switch from sonic to subsonic flow or vice versa.

Figures 21 to 23 show comparisons of baseline digital and hybrid simulation transients for the 3.048 km/M_n = 0.9, 9.144 km/M_n = 0.9, and 13.72 km/M_n = 0.9 conditions. In general, the transient results at these conditions were similar to the results obtained at the sea-level static condition. That is, the hybrid responses exhibited more fan speed overshoots (figs. 21(a), 22(a), and 23(a)) and slightly faster compressor speed responses (figs. 21(b), 22(b), and 23(b)). Figures 21 to 23 also reflect some of the steady-state differences that were discussed in the previous section. Examples of this are lower main combustor temperature and higher net thrust at 83° PLA for the 13.72 km/M_n = 0.9 condition (figs. 23(d) and (e)).

SUMMARY OF RESULTS

An existing real-time, hybrid computer simulation of the Pratt & Whitney F100-PW-100(1) turbofan engine was modified to match the predicted performance of the F100-PW-100(3) turbofan engine. The basis for the simulation modifications was the engine manufacturer's digital simulation (CCD 1103-1.0) of the F100-PW-100(3) engine. The resulting hybrid computer simulation was implemented on the Lewis Research Center's EAI model 640 digital computer, model 680 analog computer, and model 681 analog computer. The digital computer update time was approximately 7.5 milliseconds and resulted in stable, real-time operation. The digital portion of the simulation required 12 440 words of core storage (including data). Both analog computers were fully utilized.

The real-time, hybrid computer simulation of the F100-PW-100(3) turbofan engine was evaluated at a number of subsonic and supersonic flight conditions. The evaluation covered both steady-state and transient operation. The resulting hybrid simulation data were compared with baseline digital simulation results.

The steady-state evaluation showed that the hybrid simulation generally matched the baseline digital simulation within 4 percent over the F100 flight envelope. Better agreement was noted at the low altitude/low Mach number conditions since the hybrid simulation was designed to match sea-level/static data from the digital simulation.

The transient evaluation covered large changes in the pilot command at subsonic flight conditions. In general, the agreement between hybrid and digital results was good. The hybrid simulation did exhibit slightly more fan speed overshoot during accelerations. Also, the response of the hybrid-simulated compressor speed was faster than the digital response. Some of the observed transient differences could be attributed to 2 to 4 percent errors in the steady-state values at the initial, idle power settings.

The results of the evaluation indicated that the real-time, hybrid computer simulation of the F100-PW-100(3) turbofan is suitable for use in the development and evaluation of digital control systems.

Lewis Research Center,
National Aeronautics and Space Administration,
Cleveland, Ohio, April 28, 1977,
505-05.

APPENDIX A

SYMBOLS

A	cross-sectional area, cm^2
C_d	nozzle flow coefficient
c_p	specific heat at constant pressure, J/kg-K
F	thrust, N
FN7	nozzle flow function
f_i	functional relation, i = 1 to 14
f/a	local fuel-air ratio
GVIPOS	fan inlet guide vane position, deg
g_c	gravitational conversion factor, 100 cm-kg/N-sec^2
HVF	heating value of fuel, J/kg
HVSPOS	compressor stator vane position, deg
hp	turbine map enthalpy drop parameter, J/kg-$K^{1/2}$-rpm
Δh	turbine enthalpy drop, J/kg
I	polar moment of inertia, N-cm-sec^2
J	mechanical equivalent of heat, 100 N-cm/J
K_{AB}	augmentor pressure loss coefficient, N^2-sec^2/kg^2-cm^4-K
K_B	main-combustor pressure loss coefficient, N^2-sec^2/kg^2-cm^4-K
K_{BLWHT}	fraction of high-pressure-turbine cooling bleed that is performing work
K_{BLWLT}	fraction of low-pressure-turbine cooling bleed that is performing work
K_i	component temperature rise coefficient, i = 1 to 16
K_N	nozzle flow constant, kg-$K^{1/2}$/N-sec
K_{PR5}	low-pressure-turbine discharge pressure loss coefficient
l	length, cm
M_n	Mach number
N	rotational speed, rpm
P	total pressure, N/cm^2
P/P	pressure ratio

PLA	power lever angle, deg
P_s	static pressure, N/cm^2
Q	torque, N-cm
R_A	gas constant of air, 2.8699×10^4 N-cm/kg-K
REI	Reynolds number index
SMC	compressor surge margin
SMF	fan surge margin
T	total temperature, K
T/T	temperature ratio
t	time, sec
V	volume, cm^3
W	stored mass, kg
$\dot{w}$	mass flow rate, kg/sec
$\dot{w}_c$	corrected mass flow rate, kg/sec
$\dot{w}_p$	turbine map flow parameter, kg-K-cm^2/N-rpm-sec
γ	specific heat ratio
δ	total pressure relative to sea-level conditions
η	efficiency
θ	total temperature relative to standard-day conditions
τ	time constant, sec

Subscripts:

AB	augmentor
ax	axial vanes
B	main combustor
BLC	customer bleed
BLHT	high-pressure-turbine cooling bleed
BLLT	low-pressure-turbine cooling bleed
C	compressor
cm	cambered vanes
cr	critical

D	fan duct
des	design
e	nozzle exit plane
F	fuel
FAN	fan
H	high
HT	high-pressure turbine
I	inlet
ID	fan hub (core)
i	initial conditions
j	engine station (fig. 1); j = 0, 2, 2.1, 2.2, 3, 4, 4.1, 5, 6, 7, 8, 13, 16
j'	entrance to volume at station j; j = 3, 4, 4.1, 6, 7, 13, 16
L	low
LT	low-pressure turbine
M	map
m	measured
N	nozzle
n	net
OD	fan tip (bypass)
SUB	subsonic
SUP	supersonic
TPBL	turbopump bleed

APPENDIX B

SUMMARY OF EQUATIONS

$$(\dot{w}_c)_{FAN,M} = f_1\left(\frac{P_{13}}{P_2}, \frac{N_L}{\sqrt{\theta_2}}\right) \tag{B1}$$

$$\left(\frac{P}{P}\right)_{FAN,ID} = f_2\left(\frac{P_{13}}{P_2}, \frac{N_L}{\sqrt{\theta_2}}\right) \tag{B2}$$

$$\dot{w}_2 = \left\{(\dot{w}_c)_{FAN,M}\left[1. + f_{12}\left(\frac{N_L}{\sqrt{\theta_2}}, \text{ GVIPOS}\right)\right] - f_{13}(\text{REI})\right\}\frac{\delta_2}{\sqrt{\theta_2}} \tag{B3}$$

$$\text{REI} = \frac{\delta_2(T_2 + 110.33)}{398.50(\theta_2)^2} \tag{B4}$$

$$\left.\begin{aligned} f_{13} &= 0.0 && \text{if REI} \geq 0.61168 \\ &= 1.0069 - 1.6461\ \text{REI} && \text{if } 0.28404 \leq \text{REI} < 0.61168 \\ &= 3.2240 - 9.4517\ \text{REI} && \text{otherwise} \end{aligned}\right\} \tag{B5}$$

$$P_{2.1} = P_{2.2} = \left(\frac{P}{P}\right)_{FAN,ID} P_2 \tag{B6}$$

$$\left.\begin{aligned} \left(\frac{T}{T}\right)_{FAN,OD} &= K_1\frac{P_{13}}{P_2} + K_2 && \text{if } \frac{P_{13}}{P_2} \geq 2.851 \\ &= K_3\frac{P_{13}}{P_2} + K_4 && \text{if } 1.803 \leq \frac{P_{13}}{P_2} \leq 2.851 \\ &= K_5\frac{P_{13}}{P_2} + K_6 && \text{otherwise} \end{aligned}\right\} \tag{B7}$$

$$T_{13'} = \left(\frac{T}{T}\right)_{FAN,\,OD} T_2 \tag{B8}$$

$$SMF = \frac{\left[\left(\frac{P}{P}\right)_{cr,\,FAN} - \frac{P_{13}}{P_2}\right]}{\left(\frac{P}{P}\right)_{cr,\,FAN}} \tag{B9}$$

$$\left(\frac{P}{P}\right)_{cr,\,FAN} = \left(\frac{25. + GVIPOS}{25.}\right)\left(\frac{P}{P}\right)_{cr,ax,\,FAN} - \left(\frac{GVIPOS}{25.}\right)\left(\frac{P}{P}\right)_{cr,cm,\,FAN} \tag{B10}$$

$$\left(\frac{P}{P}\right)_{cr,ax,\,FAN} = 2.7372\times10^{-4}\,\frac{\dot{w}_2^2\theta_2}{\delta_2^2} + 5.1591\times10^{-4}\,\frac{\dot{w}_2\sqrt{\theta_2}}{\delta_2} + 0.77163 \tag{B11}$$

$$\left(\frac{P}{P}\right)_{cr,cm,\,FAN} = 5.3717\times10^{-4}\,\frac{\dot{w}_2^2\theta_2}{\delta_2^2} - 3.0788\times10^{-2}\,\frac{\dot{w}_2\sqrt{\theta_2}}{\delta_2} + 1.7258 \tag{B12}$$

$$\left.\begin{aligned}
\left(\frac{T}{T}\right)_{FAN,ID} &= K_7\left(\frac{P}{P}\right)_{FAN,ID} + K_8 && \text{if } \left(\frac{P}{P}\right)_{FAN,ID} \geq 2.889\\
&= K_9\left(\frac{P}{P}\right)_{FAN,ID} + K_{10} && \text{if } 1.82 \leq \left(\frac{P}{P}\right)_{FAN,ID} < 2.889\\
&= K_{11}\left(\frac{P}{P}\right)_{FAN,ID} + K_{12} && \text{otherwise}
\end{aligned}\right\} \tag{B13}$$

$$T_{2.1} = T_{2.2} = \left(\frac{T}{T}\right)_{FAN,\,ID} T_2 \tag{B14}$$

$$\left(\dot{w}_c\right)_{C,M} = f_3\left(\frac{P_3}{P_{2.2}}, \frac{N_H}{\sqrt{\theta_{2.2}}}\right) \tag{B15}$$

$$\dot{w}_{2.2} = \left(\dot{w}_c\right)_{C,M}\left[1. + f_4\left(\frac{N_H}{\sqrt{\theta_{2.2}}}, \text{HVSPOS}\right)\right]\frac{\delta_{2.2}}{\sqrt{\theta_{2.2}}} \tag{B16}$$

$$\left.\begin{aligned}\left(\frac{T}{T}\right)_C &= K_{13}\frac{P_3}{P_{2.2}} + K_{14} \qquad \text{if } \frac{P_3}{P_{2.2}} \geq 5.7407\\ &= K_{15}\frac{P_3}{P_{2.2}} + K_{16} \qquad \text{otherwise}\end{aligned}\right\} \tag{B17}$$

$$T_{3'} = \left(\frac{T}{T}\right)_C T_{2.2} \tag{B18}$$

$$\text{SMC} = \frac{\left[\left(\frac{P}{P}\right)_{cr,C} - \frac{P_3}{P_{2.2}}\right]}{\left(\frac{P}{P}\right)_{cr,C}} \tag{B19}$$

$$\left(\frac{P}{P}\right)_{cr,C} = \left(\frac{40 + \text{HVSPOS}}{44}\right)\left(\frac{P}{P}\right)_{cr,ax,C} - \left(\frac{\text{HVSPOS} - 4}{44}\right)\left(\frac{P}{P}\right)_{cr,cm,C} \tag{B20}$$

$$\left(\frac{P}{P}\right)_{cr,ax,C} = 0.00972\frac{\dot{w}_{2.2}^2\theta_{2.2}}{\delta_{2.2}^2} + 0.65235\frac{\dot{w}_{2.2}\sqrt{\theta_{2.2}}}{\delta_{2.2}} - 11.7048 \tag{B21}$$

$$\left(\frac{P}{P}\right)_{cr,cm,C} = 0.11524\frac{\dot{w}_{2.2}^2\theta_{2.2}}{\delta_{2.2}^2} - 2.9650\frac{\dot{w}_{2.2}\sqrt{\theta_{2.2}}}{\delta_{2.2}} + 24.779 \tag{B22}$$

$$\dot{w}_{BLHT} = 0.01621\ \dot{w}_{2.2} \tag{B23}$$

$$\dot{w}_{BLLT} = 0.01436\ \dot{w}_{2.2} \tag{B24}$$

$$\dot{w}_{TPBL} = 0 \tag{B25}$$

$$\left(\dot{w}_p\right)_{HT} = f_5\left(\frac{P_{4.1}}{P_4}, \frac{N_H}{\sqrt{T_4}}\right) \tag{B26}$$

$$\dot{w}_4 = \left(\dot{w}_p\right)_{HT} \frac{P_4 N_H}{T_4} \tag{B27}$$

$$(hp)_{HT} = f_6\left(\frac{P_{4.1}}{P_4}, \frac{N_H}{\sqrt{T_4}}\right) \tag{B28}$$

$$(\Delta h)_{HT} = (hp)_{HT} \sqrt{T_4}\, N_H \tag{B29}$$

$$(\dot{w}T)_{4.1'} = \dot{w}_4\left[\frac{c_{p,4}T_4}{c_{p,4.1}} - \frac{(\Delta h)_{HT}}{c_{p,4.1}}\right] + \dot{w}_{BLHT}\left[\frac{c_{p,3}T_3}{c_{p,4.1}} - \frac{K_{BLWHT}(\Delta h)_{HT}}{c_{p,4.1}}\right] \tag{B30}$$

$$\left(\dot{w}_p\right)_{LT} = f_7\left(\frac{P_5}{P_{4.1}}, \frac{N_L}{\sqrt{T_{4.1}}}\right) \tag{B31}$$

$$\dot{w}_{4.1} = \left(\dot{w}_p\right)_{LT} \frac{P_{4.1} N_L}{T_{4.1}} \tag{B32}$$

$$(hp)_{LT} = f_8\left(\frac{P_5}{P_{4.1}}, \frac{N_L}{\sqrt{T_{4.1}}}\right) \tag{B33}$$

$$(\Delta h)_{LT} = (hp)_{LT} \sqrt{T_{4.1}}\, N_L \tag{B34}$$

$$(\dot{w}T)_{6'} = \frac{\dot{w}_{13} c_{p,16} T_{16}}{c_{p,6}} + \dot{w}_{4.1}\left[\frac{c_{p,4.1}T_{4.1}}{c_{p,6}} - \frac{(\Delta h)_{LT}}{c_{p,6}}\right] + \dot{w}_{BLLT}\left[\frac{c_{p,3}T_3}{c_{p,6}} - \frac{K_{BLWLT}(\Delta h)_{LT}}{c_{p,6}}\right] \tag{B35}$$

$$\dot{w}_3 = \sqrt{\frac{P_3(P_3 - P_4)}{K_B T_3}} = \sqrt{\frac{R_A W_3(P_3 - P_4)}{K_B V_3}} \tag{B36}$$

$$(\dot{w}T)_{4'} = \frac{c_{p,3}\dot{w}_3 T_3}{c_{p,4}} + \eta_B \frac{HVF}{c_{p,4}} \dot{w}_{F,4} \tag{B37}$$

$$\eta_B \frac{HVF}{c_{p,4}} = 50362 - 7.4640\ T_4 \tag{B38}$$

$$P_{16} = P_6 \tag{B39}$$

$$P_5 = K_{PR5} P_6 \tag{B40}$$

$$P_{7'} = P_6 - \frac{K_{AB}\dot{w}_7^2 T_7}{P_6} \tag{B41}$$

$$(\dot{w}T)_{7'} = \frac{c_{p,6}}{c_{p,7}} \dot{w}_6 T_6 + \eta_{AB} \frac{HVF}{c_{p,7}} \dot{w}_{F,7} \tag{B42}$$

$$\eta_{AB} = f_9\left[\left(\frac{f}{a}\right)_7\right] \tag{B43}$$

$$\left(\frac{f}{a}\right)_7 = \frac{\dot{w}_{F,7}}{\dot{w}_6 - \dot{w}_{F,4}} \tag{B44}$$

$$P_{16'} = P_{13}\left[1 - f_{10}\left(\frac{\dot{w}_{13}\sqrt{T_{16}}}{P_{16}}\right)\right] \tag{B45}$$

$$c_{p,16} T_{16} = c_{p,13} T_{13} \tag{B46}$$

$$\left(\frac{P}{P}\right)_N = \frac{P_0}{P_7} \tag{B47}$$

$$
\begin{aligned}
FN7 &= 0.2588 && \text{if } \left(\frac{P}{P}\right)_N \le 0.53 \\
&= \left(\frac{P}{P}\right)_N^{0.7143} \sqrt{1 - \left(\frac{P}{P}\right)_N^{0.2857}} && \text{otherwise}
\end{aligned}
\quad \text{(B48)}
$$

$$
\begin{aligned}
C_{d,7} &= 0.97031 && \text{if } \left(\frac{P}{P}\right)_N < 0.3334 \\
&= 1.0645 - 0.28248\left(\frac{P}{P}\right)_N && \text{if } 0.3334 \le \left(\frac{P}{P}\right)_N < 0.3851 \\
&= 0.98563 - 0.07766\left(\frac{P}{P}\right)_N && \text{if } 0.3851 \le \left(\frac{P}{P}\right)_N < 0.4783 \\
&= 0.89488 + 0.11209\left(\frac{P}{P}\right)_N && \text{if } 0.4783 \le \left(\frac{P}{P}\right)_N < 0.8184 \\
&= 0.77344 + 0.26048\left(\frac{P}{P}\right)_N && \text{otherwise}
\end{aligned}
\quad \text{(B49)}
$$

$$
\dot{w}_7 = K_N P_7 (FN7) C_{d,7} \frac{\left[A_7 - f_{11}(T_7)\right]}{\sqrt{T_7}} \quad \text{(B50)}
$$

$$
\begin{aligned}
f_{11} &= 0 && \text{if } T_7 < 800 \\
&= 0.46870\ T_7 - 374.97 && \text{if } 800 \le T_7 < 860.6 \\
&= 0.12681\ T_7 - 80.710 && \text{if } 860.6 \le T_7 < 1200 \\
&= -0.03577\ T_7 + 114.39 && \text{if } 1200 \le T_7 < 1993 \\
&= -0.13355\ T_7 + 309.23 && \text{otherwise}
\end{aligned}
\quad \text{(B51)}
$$

$$A_8 = 1.4693\ A_7 + 0.19333\ T_7 - 1048.2 \quad \text{if } M_n < 1.1$$
$$\quad = 1.6175\ A_7 + 0.12008\ T_7 - 753.16 \quad \text{otherwise} \tag{B52}$$

$$\left(\frac{P}{P}\right)_{SUB} = 4.7317 \frac{A_8}{A_7} - 1.6486 \left(\frac{A_8}{A_7}\right)^2 - 2.5089 \tag{B53}$$

$$\left(\frac{P}{P}\right)_{SUP} = 4.7317 \frac{A_8}{A_7} + 1.6486 \left(\frac{A_8}{A_7}\right)^2 + 3.5655 \tag{B54}$$

$$\frac{P_{s,e}}{P_7} = \left(\frac{P}{P}\right)_N \quad \text{if } \left(\frac{P}{P}\right)_N \geq \left(\frac{P}{P}\right)_{SUB}$$
$$\quad = \left(\frac{P}{P}\right)_{SUP} \quad \text{otherwise} \tag{B55}$$

$$F_8 = 46.405\ \dot{w}_7 \sqrt{T_7 \left(0.2578 - 0.2578 \frac{P_{s,e}}{P_7}\right)} \quad \text{if } \left(\frac{P}{P}\right)_N \geq \left(\frac{P}{P}\right)_{SUB}$$
$$\quad = 50.996\ \dot{w}_7 \sqrt{T_7 \left[0.47303 - 1.1098 \frac{P_{s,e}}{P_7} + 0.85065 \left(\frac{P_{s,e}}{P_7}\right)^2\right]}$$
$$\quad - A_8(P_0 - P_{s,e}) \quad \text{otherwise} \tag{B56}$$

$$F_n = F_8 - 20.041\ \dot{w}_2 M_n \sqrt{T_0} \tag{B57}$$

$$W_3 = \int_0^t (\dot{w}_{2.2} - \dot{w}_{BLHT} - \dot{w}_{BLLT} - \dot{w}_{TPBL} - \dot{w}_{BLC} - \dot{w}_3)\, dt + W_{3,i} \tag{B58}$$

$$T_3 = \frac{1}{\tau_3} \int_0^t (T_{3'} - T_3)\, dt + T_{3,i} \tag{B59}$$

$$P_3 = \frac{R_A W_3 T_3}{V_3} \tag{B60}$$

$$W_4 = \int_0^t (\dot{w}_3 + \dot{w}_{F,4} - \dot{w}_4)\, dt + W_{4,i} \tag{B61}$$

$$P_4 = \frac{R_A \gamma_4}{V_4} \int_0^t \left[(\dot{w}T)_{4'} - \dot{w}_4 T_4\right] dt + P_{4,i} \tag{B62}$$

$$T_4 = \frac{V_4 P_4}{R_A W_4} \tag{B63}$$

$$W_{4.1} = \int_0^t (\dot{w}_4 + \dot{w}_{BLHT} - \dot{w}_{4.1})\, dt + W_{4.1,i} \tag{B64}$$

$$P_{4.1} = \frac{R_A \gamma_{4.1}}{V_{4.1}} \int_0^t \left[(\dot{w}T)_{4.1'} - \dot{w}_{4.1} T_{4.1}\right] dt + P_{4.1,i} \tag{B65}$$

$$T_{4.1} = \frac{V_{4.1} P_{4.1}}{R_A W_{4.1}} \tag{B66}$$

$$W_{13} = \int_0^t (\dot{w}_2 - \dot{w}_{2.2} - \dot{w}_{13})\, dt + W_{13,i} \tag{B67}$$

$$T_{13} = \frac{1}{\tau_{13}} \int_0^t (T_{13'} - T_{13})\, dt + T_{13,i} \tag{B68}$$

$$P_{13} = \frac{R_A}{V_{13}} W_{13} T_{13} \tag{B69}$$

$$W_6 = \int_0^t (\dot{w}_{13} + \dot{w}_{4.1} + \dot{w}_{BLLT} + \dot{w}_{TPBL} - \dot{w}_6)\, dt + W_{6,i} \tag{B70}$$

$$P_6 = \frac{R_A \gamma_6}{V_6} \int_0^t \left[(\dot{w}T)_{6'} - \dot{w}_6 T_6\right] dt + P_{6,i} \tag{B71}$$

$$T_6 = \frac{V_6 P_6}{R_A W_6} \tag{B72}$$

$$W_7 = \int_0^t (\dot{w}_6 + \dot{w}_{F,7} - \dot{w}_7)\, dt + W_{7,i} \tag{B73}$$

$$P_7 = \frac{R_A \gamma_7}{V_7} \int_0^t \left[(\dot{w}T)_{7'} - \dot{w}_7 T_7\right] dt + P_{7,i} \tag{B74}$$

$$T_7 = \frac{V_7 P_7}{R_A W_7} \tag{B75}$$

$$\dot{w}_{13} = \left(\frac{Ag_c}{l}\right)_D \int_0^t (P_{16'} - P_{16})\, dt + \dot{w}_{13,i} \tag{B76}$$

$$\dot{w}_6 = \left(\frac{Ag_c}{l}\right)_{AB} \int_0^t (P_{7'} - P_7)\, dt + \dot{w}_{6,i} \tag{B77}$$

$$(NQ)_{HT} = \frac{30J}{\pi} (\Delta h)_{HT}(\dot{w}_4 + K_{BLWHT}\dot{w}_{BLHT}) \tag{B78}$$

$$(NQ)_C = \frac{30J}{\pi} c_{p,2.2}\dot{w}_{2.2}\left[\left(\frac{c_{p,3'}}{c_{p,2.2}}\right)T_{3'} - T_{2.2}\right] \tag{B79}$$

$$\left(\frac{c_{p,3'}}{c_{p,2.2}}\right) = 1.0815^{*} + 0.00008\ T_3 - 0.00033\ T_2 - 0.00038\ P_2 \tag{B80}$$

---

* Adjusted, if necessary, to match rotor speeds at PLA = 83°.

$$N_H = \frac{30}{\pi I_H} \int_0^t \left[\frac{(NQ)_{HT} - (NQ)_C}{N_H}\right] dt + N_{H,i} \tag{B81}$$

$$(NQ)_{LT} = \frac{30J}{\pi} (\Delta h)_{LT}(\dot{w}_{4.1} + K_{BLWLT}\dot{w}_{BLLT}) \tag{B82}$$

$$(NQ)_{FAN,\,OD} = \frac{30J}{\pi} c_{p,2}(\dot{w}_2 - \dot{w}_{2.2})\left(\frac{c_{p,13'}}{c_{p,2}} T_{13'} - T_2\right) \tag{B83}$$

$$(NQ)_{FAN,\,ID} = \frac{30J}{\pi} c_{p,2.2}\dot{w}_{2.2}\left[\left(\frac{c_{p,2.2}}{c_{p,2}}\right) T_{2.2} - T_2\right] \tag{B84}$$

$$\left(\frac{c_{p,2.2}}{c_{p,2}}\right) = 1.0515^{*} - 0.00011\ T_{2.2} + 0.00012\ T_2 - 0.00159\ P_2 \tag{B85}$$

$$N_L = \frac{30}{\pi I_L} \int_0^t \left[\frac{(NQ)_{LT} - (NQ)_{FAN,\,OD} - (NQ)_{FAN,\,ID}}{N_L}\right] dt + N_{L,i} \tag{B86}$$

$$\left(\frac{P_{13} - P_{s,13}}{P_{13}}\right) = f_{14}\left(\frac{\dot{w}_{13}\sqrt{T_{13}}}{P_{13}A_{13}}\right) \tag{B87}$$

$$\left(\frac{P_{2.1} - P_{s,2.1}}{P_{2.1}}\right) = f_{14}\left(\frac{\dot{w}_{2.2}\sqrt{T_{2.2}}}{P_{2.2}A_{2.2}}\right) \tag{B88}$$

---

*Adjusted, if necessary, to match rotor speeds at PLA = 83°.

APPENDIX C

DIGITAL PROGRAM

FORTRAN Listing

```
C*****ADC VARIABLES
      SCALED FRACTION X0,X1,X2,X3,X4,X5,X6,X7,X8,X9,X10,X11
      SCALED FRACTION X12,X13,X14,X15,X16,X17,X18,X19,X20,X21,X22
      SCALED FRACTION X23
C*****DAC VARIABLES
      SCALED FRACTION Y0,Y1,Y2,Y3,Y4,Y5,Y6,Y7,Y8,Y9,Y10,Y11,Y12
C*****OTHER VARIABLES
      SCALED FRACTION XVALS(10,8,6),YVALS(8,6),ZVALS(10,8,12),YI(24),
     1 V9,V10,SSQRT,MAP2,MAP2L,V3,V4,V5,AR,PRSUB,DPR,PE,PRE,
     2 PRSUP,FRD,V6,V7,V8,RT4,RT41,AE,A,DY7,V11,REY,PRF1,PRF2,PRC1,
     3 PRC2,Y6SQ,Y7SQ
      COMMON/MAPS/XVALS,YVALS,ZVALS,IX(6),JY(6),NX(6),NY(6),KX(6),KY(6)
      COMMON/IDAC/YI
      LOGICAL SENSW,READY
      REAL M0
      CALL QSHYIN(IERR,680,680)
      TYPE 5
    5 FORMAT(3X,21HTYPE DATE AS 03-10-75//)
      ACCEPT 6,DATE1,DATE2
    6 FORMAT(2A4)
C*****SPECIFY FLIGHT CONDITION FOR ENGINE
    7 TYPE 11
      ACCEPT 12,P0,T0,M0
C*****INITIALIZE DACS
  100 CALL QSC(0,IERR)
      CALL QSC(1,IERR)
  105 CALL QWBDAS(YI,0,24,IERR)
      CALL QSTDA
      DO 106  K=1,16
      KK=K-1
      CALL QWCLL(KK,.FALSE.,IERR)
  106 CONTINUE
   11 FORMAT(/3X,33HTYPE DESIRED VALUES FOR P0,T0,M0./)
   12 FORMAT(F7.3,F8.3,F5.2)
      P0SI= P0*.68948
      T0SI= T0*.55555
      V3= P0/20.
      V5=M0/3.
      V6=T0/1000.
      V11=V5*SSQRT(V6)
C*****PLACE ANALOG IN IC MODE
   19 TYPE 20
   20 FORMAT(3X,48HSLAVE CONSOLE 2 TO CONSOLE 1.  MANUALLY GO TO IC./)
      TYPE 21
   21 FORMAT(/3X,44HPROCEED TO DYNAMIC PART OF PROGRAM BY R-S-R./)
      PAUSE
C*****READ ADC VALUES AND GENERATE MAP OUTPUTS
   22 CALL QRBADS(X0,0,5,IERR)
      Y7=MAP2(4,X3,X4)
```

```
      Y5=MAP2L(7)
      IF(X2.GT..05S) X2=.05S
      A=MAP2(1,X4,-X2)
      Y7=(Y7*(.5S+.5S*A))/.5S
      DY7=.0S
      REY=(.56715S*X0*(.9S*X1+.17874S))/(X1*X1)
      IF(REY.LT..30584S) DY7=-.02626S*REY+.00803S
      IF(REY.LT..14202S) DY7=-.15077S*REY+.02571S
      Y7=Y7-DY7
      Y3=Y7
      CALL QWJDAS(Y3,3,IERR)
      CALL QWJDAS(Y5,5,IERR)
      CALL QWJDAS(Y7,7,IERR)
      CALL QRBADS(X5,5,3,IERR)
      IF(X5.GT..00000S)  X5=.00000S
      V4=MAP2(2,X6,-X5)
      Y6=MAP2(3,X7,X6)
      Y6=(Y6*(.5S+.5S*V4))/.5S
      Y2=Y6
      CALL QWJDAS(Y2,2,IERR)
      CALL QWJDAS(Y6,6,IERR)
  223 CALL QRBADS(X8,8,3,IERR)
      RT4=SSQRT(X8)
      V7=(.79567S*X10)/RT4
      Y8-MAP2(5,X9,V7)
      V9=MAP2L(8)
      Y9=(-V9*RT4)/.78259S
      CALL QWJDAS(Y8,8,IERR)
      CALL QWJDAS(Y9,9,IERR)
  224 CALL QRBADS(X11,11,3,IERR)
      RT41=SSQRT(X12)
      V8=(.82695S*X11)/RT41
      Y10=MAP2(6,X13,V8)
      V10=MAP2L(9)
      Y11=(-V10*RT41)/.46715S
      CALL QWJDAS(Y10,10,IERR)
      CALL QWJDAS(Y11,11,IERR)
  225 CALL QRBADS(X22,22,2,IERR)
      Y4=X22*X23
      CALL QWJDAS(Y4,4,IERR)
  226 CALL QRBADS(X14,14,5,IERR)
      IF(V5.GT..36667S)  GO TO 2265
      AE=.04162S*X14-.08124S+.73465S*X17
      GO TO 2266
 2265 AE=.02585S*X14-.05837S+.80875S*X17
 2266 AR=AE/X17
      DPR=(.69683S*AR*AR-AR+.32094S)/.10567S
      PRSUB=.52828S-DPR
      PE=PRSUB*X18
      FRD=.75722S*X16*V11
      IF(.20000S*V3.LT.PE) GO TO 227
      PRE=.20000S*V3/X18
      Y12=((X15*SSQRT((.2578S-.2578S*PRE)+X14))/.7652S-FRD)
     1 /.34933S
      GO TO 228
  227 PRSUP=.52828S+DPR
      PE=PRSUP*X18
      Y12=((X15*SSQRT((.47303S-PRSUP/.90106S+.85065S*PRSUP*PRSUP)
     1 *X14))/.69633S-FRD-(AE*(.20000S*V3-PE))/.4293S)/.34933S
```

```
228 Y7SQ=Y7*Y7
     PRF1=.76979S*Y7SQ+.01157S*Y7+.13800S
     PRF2=(.90645S*Y7SQ-.41427S*Y7+.18519S)/.8S
     Y0=(.75S*PRF1*(.99999S+X2)-X2*PRF2)/.75S
     Y0=(Y0-.83333S*X3)/Y0
     Y6SQ=Y6*Y6
     PRC1=(.29113S*Y6SQ-.46385S+.7107S*Y6)/.6S
     PRC2=(.86275S*Y6SQ-.80752S*Y6+.24549S)/.25S
     Y1=(.6S*PRC1*(.99999S+X5)-X5*PRC2)/.6S
     Y1=(Y1-.83333S*X7)/Y1
 23  CALL QWJDAS(Y12,12,IERR)
     CALL QWJDAS(Y0,0,IERR)
     CALL QWJDAS(Y1,1,IERR)
C*****OUTPUT UNSCALED DATA AT TELETYPE IF DESIRED
     IF(.NOT.SENSW(1)) GO TO 22
     CALL QRAMI(ILOC)
     CALL QSC(2,IERR)
     CALL QSH(IERR)
     CALL QSC(0,IERR)
     CALL QSC(1,IERR)
     CALL QRBADS(X19,19,3,IERR)
     CALL QSC(2,IERR)
     P13Q2=X3
     P13Q2=P13Q2*1.5*3.1064
     XNLR2=X4
     XNLR2=XNLR2*1.2*10289.
     P3Q22=X7
     P3Q22=P3Q22*1.5*8.4113
     XNHR22=X6
     XNHR22=XNHR22*1.1*10777.
     P41Q4=X9
     P41Q4=P41Q4*3.0*.27448
     CNHPT = V7
     CNHPT=CNHPT*1.25*238.47
     CNHTSI =CNHPT*1.3416
     P5Q41=X13
     P5Q41=P5Q41*2.5*.44355
     CNLPT = V8
     CNLPT=CNLPT*1.5*220.80
     CNLTSI= CNLPT*1.3416
     GVIPOS=X?
     GVIPOS=GVIPOS*25.
     HVSPOS=X5
     HVSPOS=HVSPOS*44.+4.0
     P2=X0
     P2=P2*40.
     P2SI=P2*.68948
     T2=X1
     T2=T2*1000.
     T2SI=T2*.55555
     WF4=X22
     WF4=WF4*4.5833
     WF4SI= WF4*.45359
     WF4=WF4*3600.
     AN=X17
     AN = AN*1000.
     ANSI = AN*.00064516
     AN=AN/144.
```

```
      P4=X21
      P4=P4+600
      P4SI=P4*.68948
      XNL=X11
      XNL= XNL*15000.
      XNH=X10
      XNH= XNH*15000.
      T4=X8
      T4= T4*4000.
      T4SI= T4*.55555
      PLA = X19
      PLA= PLA*150.
      T7=X14
      T7 = T7*5000
      T7SI= T7*.55555
      WF7 = X20
      WF7 = WF7*20.
      WF7SI= WF7*.45359
      WF7=WF7*3600.
      WA2=X16
      WA2=WA2*450
      WA2SI=WA2*.45359
      T41=X12
      T41=T41*3000.
      T41SI=T41*.55555
      P2102= Y5
      P2102=P2102*1.5*3.0986
      WAR22= Y6
      WAR22=WAR22*1.1*55.097
      WR22SI= WAR22*.45359
      WAR2 = Y7
      WAR2=WAR2*1.2*230.38
      WAR2SI= WAR2*.45359
      WPHPT= Y8
      WPHPT=WPHPT*1.50*.073872
      WPHTSI= WPHPT*.36548
      HPHPT = Y9
      HPHPT=HPHPT*1.50*.28060
      HPHTSI= HPHPT*3118.7
      WPLPT= Y10
      WPLPT=WPLPT*2.5*.29326
      WPLTSI=WPLPT*.36548
      HPLPT=V10
      HPLPT=HPLPT*2.5*.20852
      HPLTSI= HPLPT*3118.7
      FN=Y12
      FN=FN*30000.
      FNSI=FN*4.4482E-3
      REYI=REY
      REYI=REYI*2.
      TYPE 24,DATE1,DATE2
   24 FORMAT(21X,33HF100 SIMULATION STEADY-STATE DATA,5X,5HDATE:,
     1 2A4///)
      IF(.NOT.SENSW(2)) GO TO 441
      TYPE 25,P0SI,P0
   25 FORMAT(5X,9HP0      = ,F7.3,9X,7HN/SQ CM,7X,2H( ,F7.3,9X,8HPSIA    )
     1)
      TYPE 26,T0SI,T0
   26 FORMAT(5X,9HT0      = ,F7.2,9X,7HK      ,7X,2H( ,F7.2,9X,8HR       )
```

```
    1)
     TYPE 27,HO
 27 FORMAT(5X,9HHO       = ,F7.4)
     TYPE 28,P2SI,P2
 28 FORMAT(5X,9HP2       = ,F7.3,9X,7HN/SQ CM,7X,2H( ,F7.3,9X,8HPSIA    )
    1)
     TYPE 29,T2SI,T2
 29 FORMAT(5X,9HT2       = ,F7.2,9X,7HK      ,7X,2H( ,F7.2,9X,8HR       )
    1)
     TYPE 295,REYI
295 FORMAT(5X,9HREYI     = ,F7.4)
     TYPE 30,PLA
 30 FORMAT(5X,9HPLA      = ,F7.2,9X,3HDEG)
     TYPE 31,WF4SI,WF4
 31 FORMAT(5X,9HWF4      = ,F7.4,9X,7HKG/SEC ,7X,2H( ,F7.0,9X,8HLBM/HR )
    1)
     TYPE 32,WF7SI,WF7
 32 FORMAT(5X,9HWF7      = ,F7.3,9X,7HKG/SEC ,7X,2H( ,F7.0,9X,8HLBM/HR )
    1)
     TYPE 33,GVIPOS
 33 FORMAT(5X,9HGVIPOS = ,F7.3,9X,3HDEG)
     TYPE 34,HVSPOS
 34 FORMAT(5X,9HHVSPOS = ,F7.3,9X,3HDEG)
     TYPE 35,ANSI,AN
 35 FORMAT(5X,9HAN       = ,F7.5,9X,7HSQ M   ,7X,2H( ,F7.4,9X,8HSQ FT   )
    1)
     TYPE 36,XNH
 36 FORMAT(5X,9HXNH      = ,F7.0,9X,3HRPM)
     TYPE 37,XNL
 37 FORMAT(5X,9HXNL      = ,F7.0,9X,3HRPM)
     TYPE 38,WA2SI,WA2
 38 FORMAT(5X,9HWA2      = ,F7.2,9X,7HKG/SEC ,7X,2H( ,F7.2,9X,8HLBM/SEC)
    1)
     TYPE 40,P4SI,P4
 40 FORMAT(5X,9HP4       = ,F7.2,9X,7HN/SQ CM,7X,2H( ,F7.2,9X,8HPSIA    ),
    1)
     TYPE 41,FNSI,FN
 41 FORMAT(5X,9HFN       = ,F7.2,9X,7HKN     ,7X,2H( ,F7.0,9X,8HLBF     )
    1)
     TYPE 42,T4SI,T4
 42 FORMAT(5X,9HT4       = ,F7.1,9X,7HK      ,7X,2H( ,F7.1,9X,8HR       )
    1)
     TYPE 39,T41SI,T41
 39 FORMAT(5X,9HT41      = ,F7.1,9X,7HK      ,7X,2H( ,F7.1,9X,8HR       )
    1)
     TYPE 43,T7SI,T7
 43 FORMAT(5X,9HT7       = ,F7.1,9X,7HK      ,7X,2H( ,F7.1,9X,8HR       )
    1)
     TYPE 45,P13Q2
     IF(.NOT.SENSW(3))  GO TO 60
 45 FORMAT(5X,9HP13Q2  = ,F7.4)
441 TYPE 46,XNLR2
 46 FORMAT(5X,9HXNLR2  = ,F7.0,9X,3HRPM)
     TYPE 47,WAR2SI,WAR2
 47 FORMAT(5X,9HWAR2     = ,F7.2,9X,7HKG/SEC ,7X,2H( ,F7.2,9X,8HLBM/SEC)
    1)
     TYPE 48,P21Q2
```

```
 48 FORMAT(5X,9HP2102   = ,F7.4)
    TYPE 49,P3022
 49 FORMAT(5X,9HP3022   = ,F7.3)
    TYPE 50,XNHR22
 50 FORMAT(5X,9HXNHR22 = ,F7.0,9X,3HRPM)
    TYPE 51,WR22SI,WAR22
 51 FORMAT(5X,9HWAR22   = ,F7.2,9X,7HKG/SEC ,7X,2H( ,F7.2,9X,8HLBM/SEC)
   1)
    TYPE 52,P4104
 52 FORMAT(5X,9HP4104   = ,F7.5)
    TYPE 53,CNHTSI,CNHPT
 53 FORMAT(5X,9HCNHPT   = ,F7.2,9X,7H       ,7X,2H( ,F7.2,9X,8H        )
   1)
    TYPE 54,WPHTSI,WPHPT
 54 FORMAT(5X,9HWPHPT   = ,F7.5,9X,7H       ,7X,2H( ,F7.5,9X,8H        )
   1)
    TYPE 55,HPHTSI,HPHPT
 55 FORMAT(5X,9HHPHPT   = ,F7.1,9X,7H       ,7X,2H( ,F7.5,9X,8H        )
   1)
    TYPE 56,P5041
 56 FORMAT(5X,9HP5041   = ,F7.5)
    TYPE 57,CNLTSI,CNLPT
 57 FORMAT(5X,9HCNLPT   = ,F7.2,9X,7H       ,7X,2H( ,F7.2,9X,8H        )
   1)
    TYPE 58,WPLTSI,WPLPT
 58 FORMAT(5X,9HWPLPT   = ,F7.5,9X,7H       ,7X,2H( ,F7.5,9X,8H        )
   1)
    TYPE 59,HPLTSI,HPLPT
 59 FORMAT(5X,9HHPLPT   = ,F7.1,9X,7H       ,7X,2H( ,F7.5,9X,8H        )
   1)
    TYPE 591,Y0
591 FORMAT(5X,9HSMF     = ,S7)
    TYPE 592,Y1
592 FORMAT(5X,9HSMC     = ,S7)
 60 IF(ILOC.EQ.6)  GO TO 61
    CALL QSOP(IERR)
    GO TO 62
 61 CALL QSIC(IERR)
 62 CALL QSC(0,IERR)
    CALL QSC(1,IERR)
    GO TO 22
    END
```

FORTRAN Symbols

A	shift in fan map corrected airflow due to change in inlet guide vane position (scaled)
AE	exhaust nozzle exit area (scaled)
AN	exhaust nozzle throat area, ft^2
ANSI	exhaust nozzle throat area, m^2
AR	exhaust nozzle expansion ratio (scaled)
CNHPT	high-pressure-turbine corrected speed, $rpm/{}^{o}R^{1/2}$
CNHTSI	high-pressure-turbine corrected speed, $rpm/K^{1/2}$
CNLPT	low-pressure-turbine corrected speed, $rpm/{}^{o}R^{1/2}$
CNLTSI	low-pressure-turbine corrected speed, $rpm/K^{1/2}$
DPR	shift in critical pressure ratio due to expansion ratio
DY7	shift in fan map corrected airflow due to change in Reynolds number (scaled)
FN	net thrust (uninstalled), lbf
FNSI	net thrust (uninstalled), kN
FRD	ram drag (scaled)
GVIPOS	inlet guide vane position, deg
HPHPT	high-pressure-turbine enthalpy drop parameter, $Btu/lbm\text{-}{}^{o}R^{1/2}\text{-}rpm$
HPHTSI	high-pressure-turbine enthalpy drop parameter, $J/kg\text{-}K^{1/2}\text{-}rpm$
HPLPT	low-pressure-turbine enthalpy drop parameter, $Btu/lbm\text{-}{}^{o}R^{1/2}\text{-}rpm$
HPLTSI	low-pressure-turbine enthalpy drop parameter, $J/kg\text{-}K^{1/2}\text{-}rpm$
HVSPOS	stator vane position, deg
IERR	error flag for linkage routines
IX	array containing number of points per curve for each map pair
JY	array containing number of curves for each map pair
K	control line initialization index
KK	K-1
KX	array containing x out-of-range counts for each map pair
KY	array containing y out-of-range counts for each map pair
MAP2	bivariate function (first function)

MAP2L	bivariate function (second function)
MO	Mach number
NX	array containing number of points per curve for each map pair
NY	array containing number of curves for each map pair
PE	exhaust plane pressure (scaled)
PLA	power lever angle, deg
PRC1	compressor critical pressure ratio, axial vanes (scaled)
PRC2	compressor critical pressure ratio, cambered vanes (scaled)
PRE	nozzle pressure ratio
PRF1	fan critical pressure ratio, axial vanes (scaled)
PRF2	fan critical pressure ratio, cambered vanes (scaled)
PRSUB	critical nozzle pressure ratio
PRSUP	design pressure ratio for supersonic nozzle flow
PI	pressure at station I, psia
PISI	pressure at station I, N/cm^2
PJQI	ratio of pressure at station J to pressure at station I
QRAMI	linkage routine for sensing analog mode
QRBADS	linkage routine for reading ADC's
QSC	linkage routine for selecting analog console
QSH	linkage routine for placing analog console in HOLD mode
QSIC	linkage routine for placing analog console in IC mode
QSHYIN	linkage routine for addressing analog consoles
QSOP	linkage routine for placing analog console in OPERATE mode
QSTDA	linkage routine for transferring DAC data
QWBDAS	linkage routine for loading DAC's
QWCLL	linkage routine for setting control lines
QWJDAS	linkage routine for "JAMMING" DAC's
REY	Reynold's number index (scaled)
REYI	Reynolds number index
RT4	square root of T4 (scaled)

RT41	square root of T41 (scaled)
SENSW	array containing logical indication of sense switch positions
SSQRT	scaled-fraction square root routine
TI	temperature at station I, °R
TISI	temperature of station I, K
TJQI	ratio of temperature at station J to temperature at station I
V3	ambient pressure (scaled)
V4	shift in compressor map corrected airflow due to change in stator vane position (scaled)
V5	Mach number (scaled)
V6	ambient temperature (scaled)
V7	high-pressure-turbine corrected speed (scaled)
V8	low-pressure-turbine corrected speed (scaled)
V9	high-pressure-turbine enthalpy drop parameter (scaled)
V10	low-pressure-turbine enthalpy drop parameter (scaled)
V11	product of Mach number and square root of ambient temperature (scaled)
WA2	fan airflow, lbm/sec
WA2SI	fan airflow, kg/sec
WAR2	fan corrected airflow, lbm/sec
WAR22	compressor corrected airflow, lbm/sec
WAR2SI	fan corrected airflow, kg/sec
WF4	main-combustor fuel flow, lbm/hr
WF4SI	main-combustor fuel flow, kg/hr
WF7	augmentor fuel flow, lbm/hr
WF7SI	augmentor fuel flow, kg/hr
WPHPT	high-pressure-turbine corrected flow, lbm-°R-in.^{2}/lbf-rpm-sec
WPHTSI	high-pressure-turbine corrected flow, kg-K-cm^2/N-rpm-sec
WPLPT	low-pressure-turbine corrected flow, lbm-°R-in.^{2}/lbf-rpm-sec
WPLTSI	low-pressure-turbine corrected flow, kg-K-cm^2/N-rpm-sec
WR22SI	compressor corrected airflow, kg/sec

XNH	high-speed-rotor speed, rpm
XNHR22	compressor corrected speed, rpm
XNL	low-speed-rotor speed, rpm
XNLR2	fan corrected speed, rpm
XVALS	array containing scaled map input x data
XI	variable read on ADC channel I
YVALS	array containing scaled map input y data
YI	variable output of DAC channel I
Y6SQ	output of DAC channel 6 squared
Y7SQ	output of DAC channel 7 squared
ZVALS	array containing scaled map output z data

APPENDIX D

ANALOG PATCHING DIAGRAMS

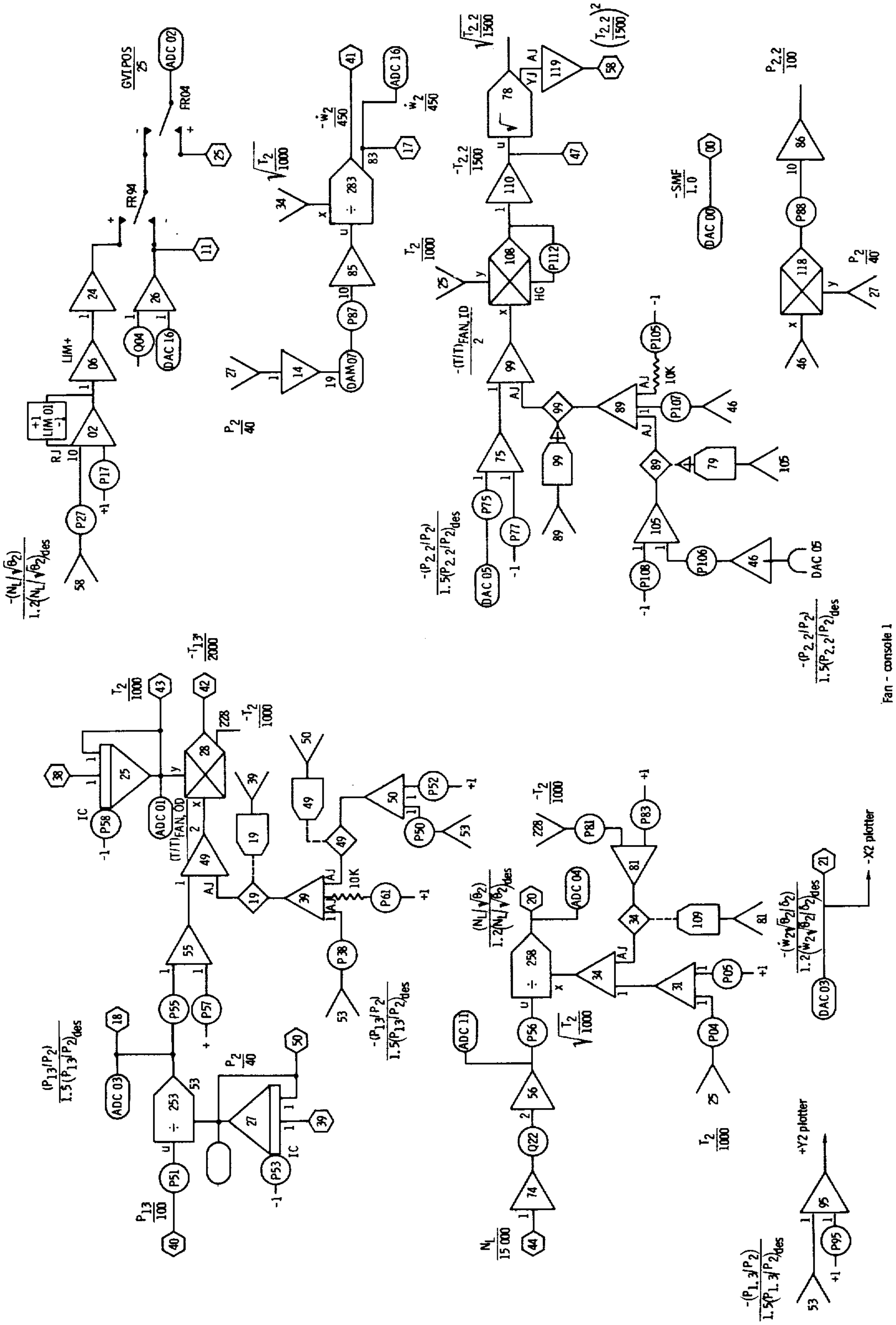

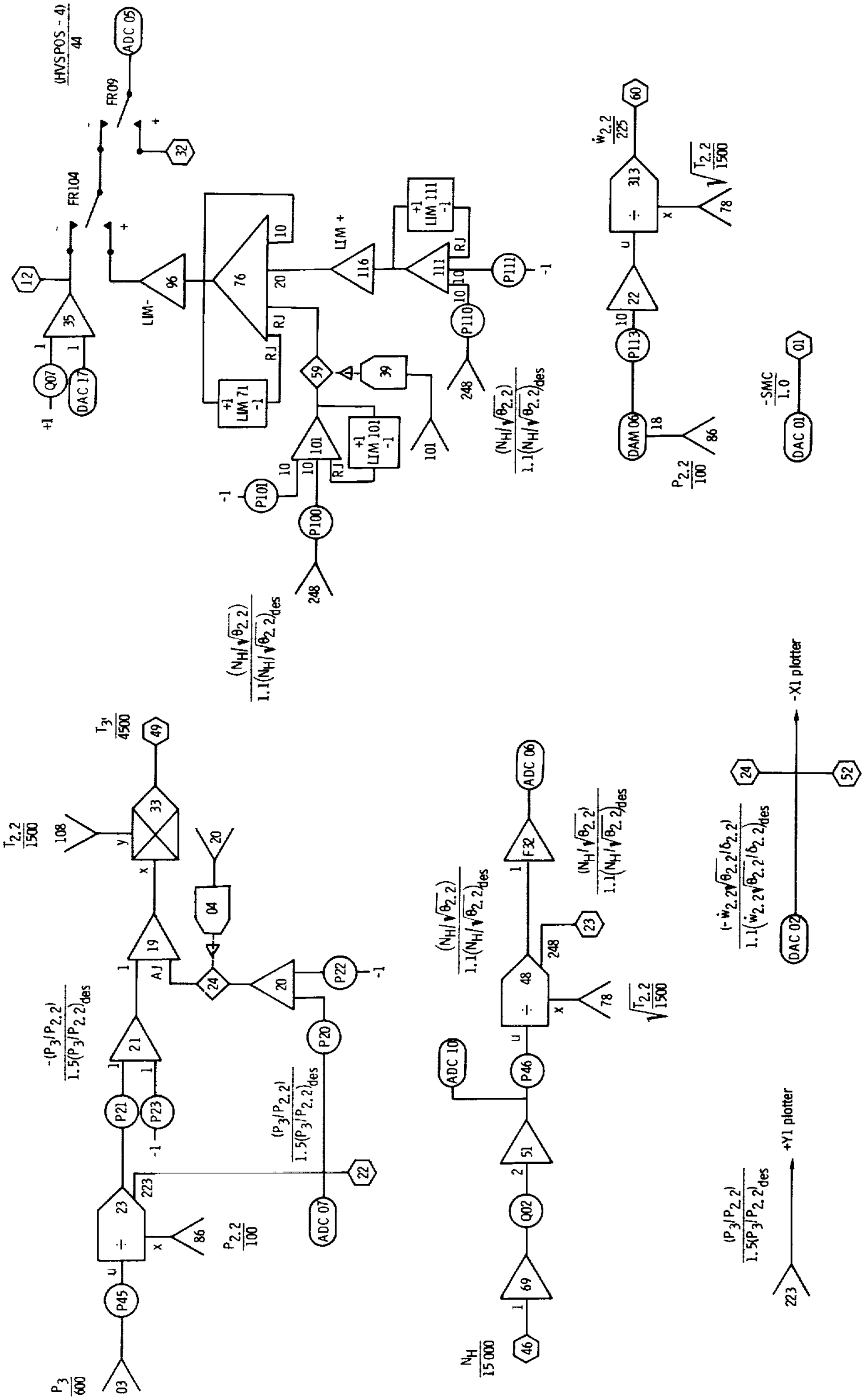

Compressor - console 1

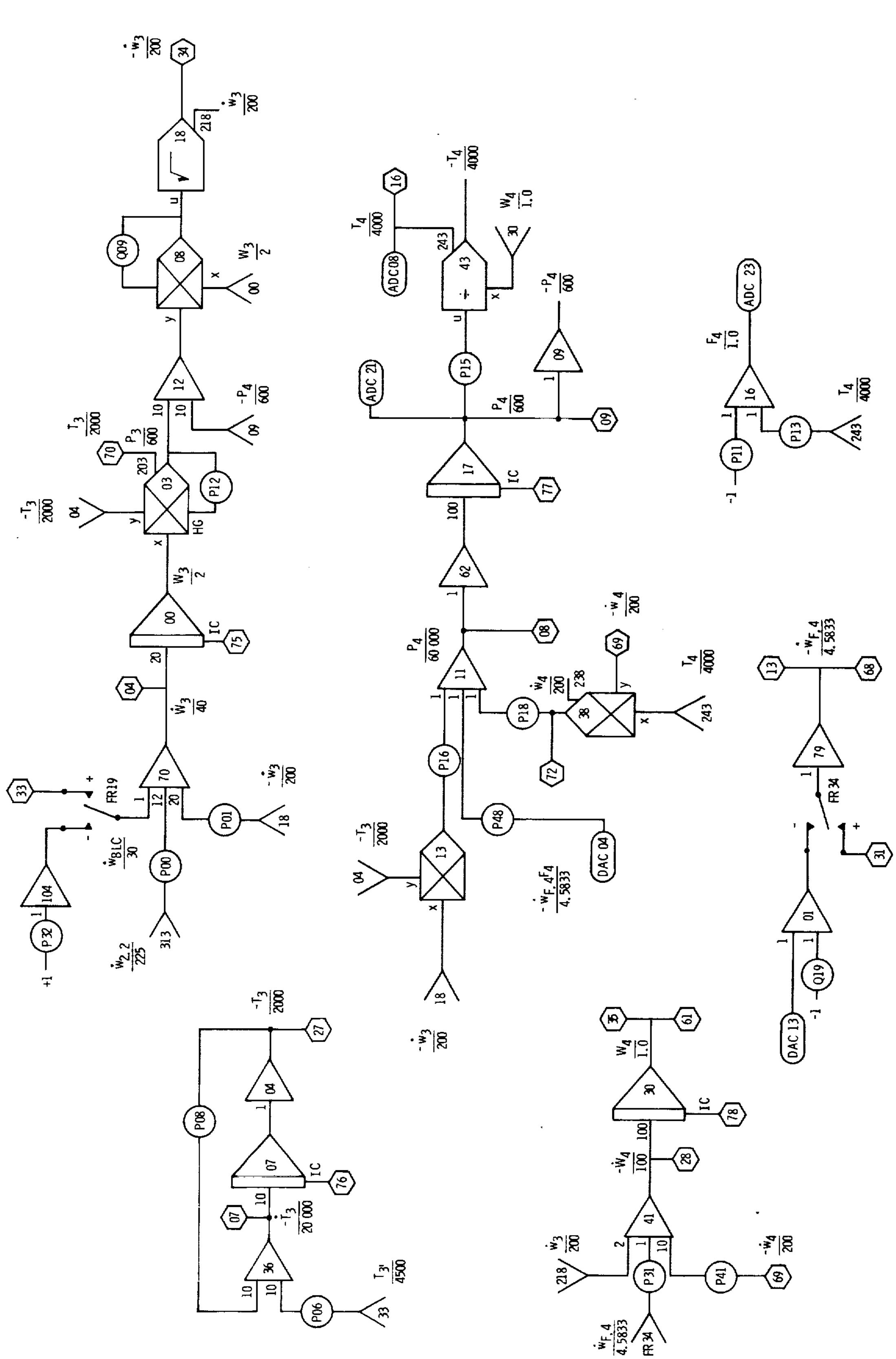

Main combustor - console 1

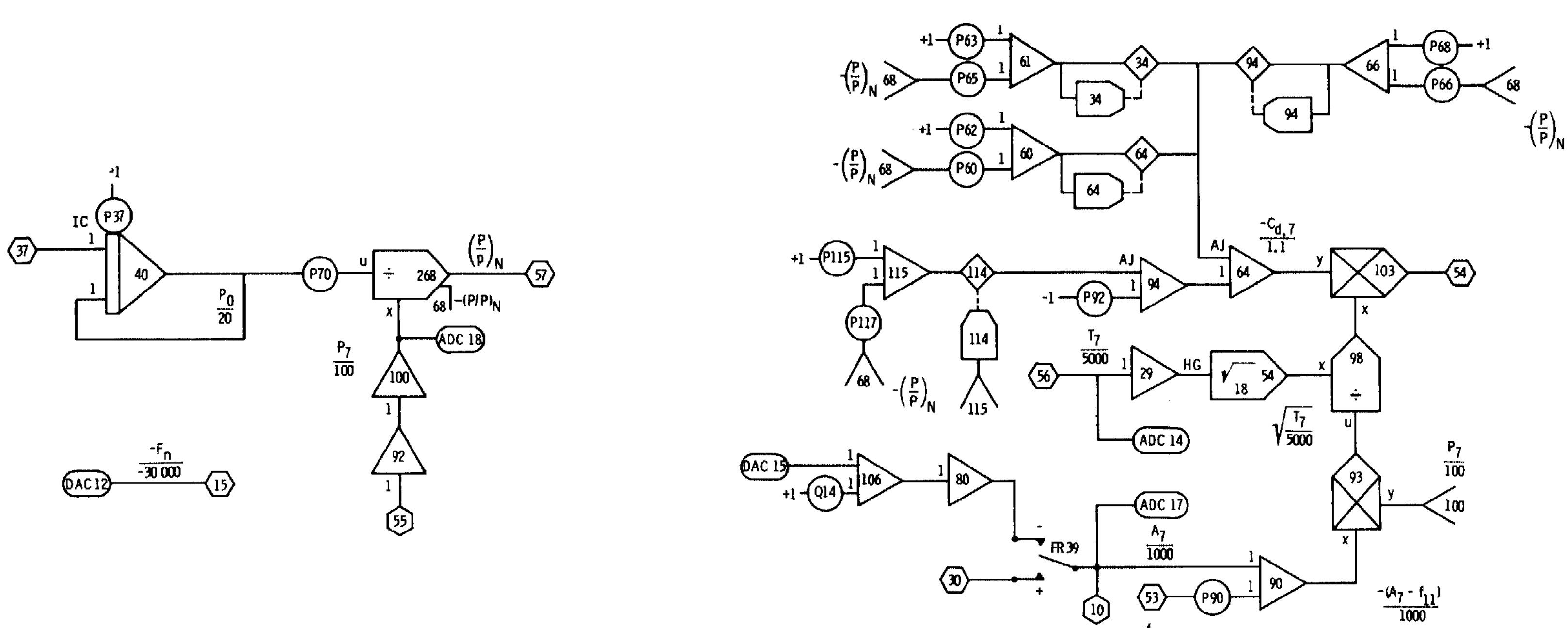

Nozzle - console 1

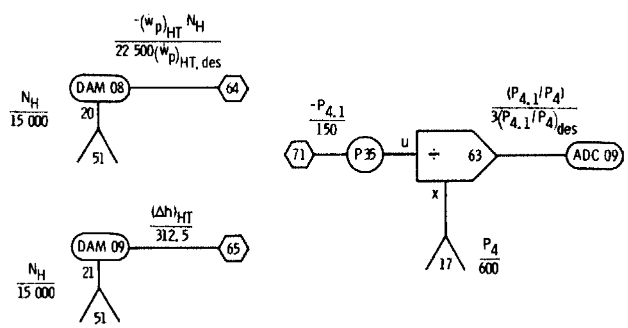

High pressure turbine - console 1

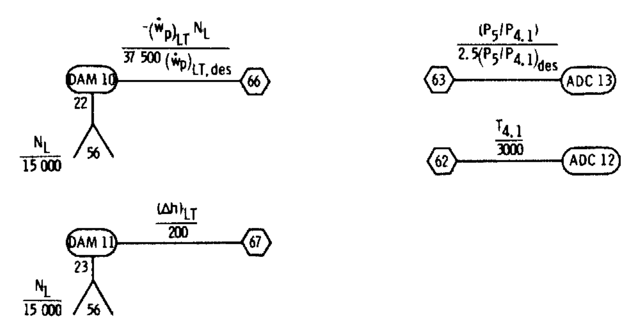

Low pressure turbine - console 1

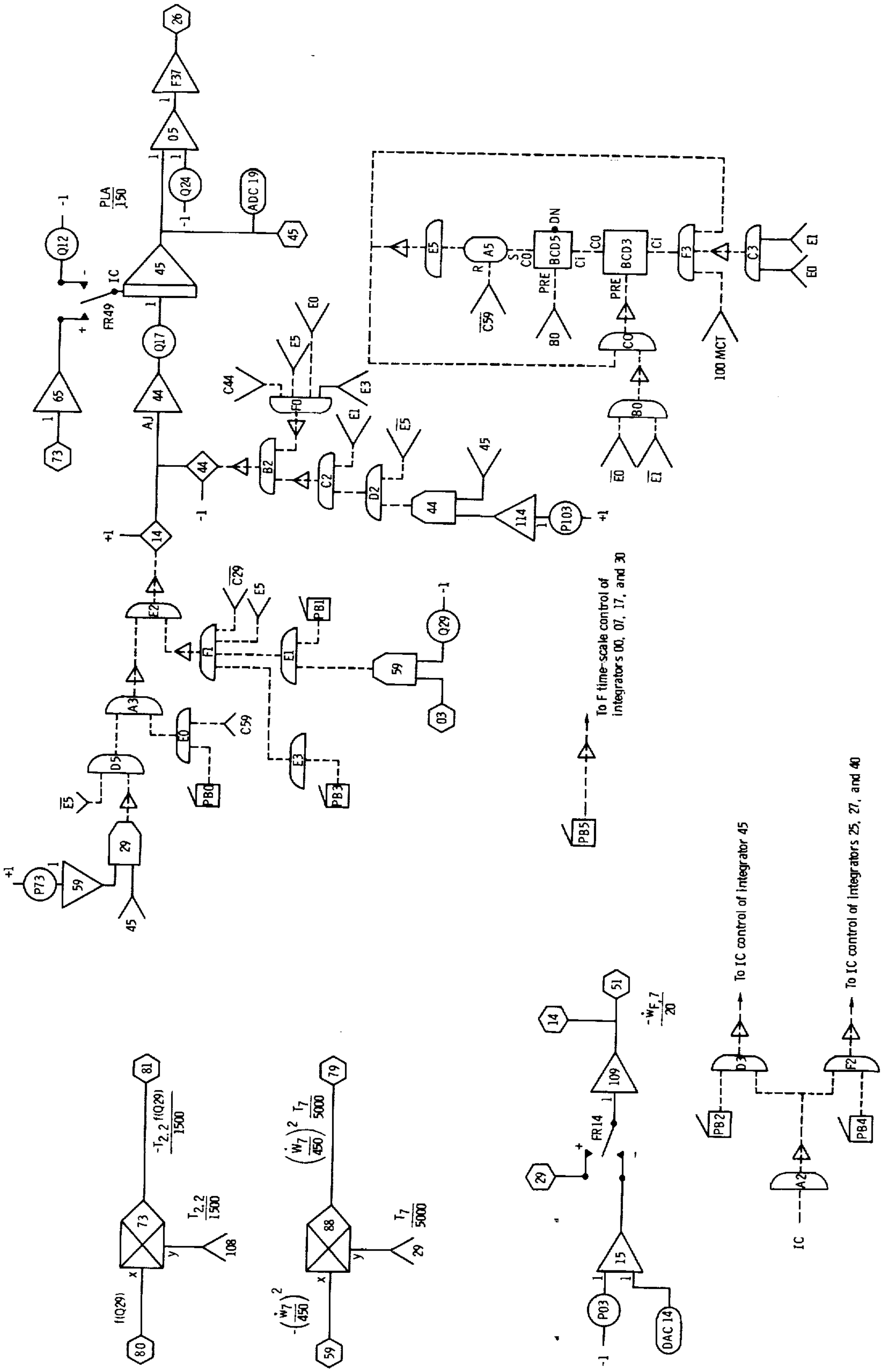

Miscellaneous - console 1

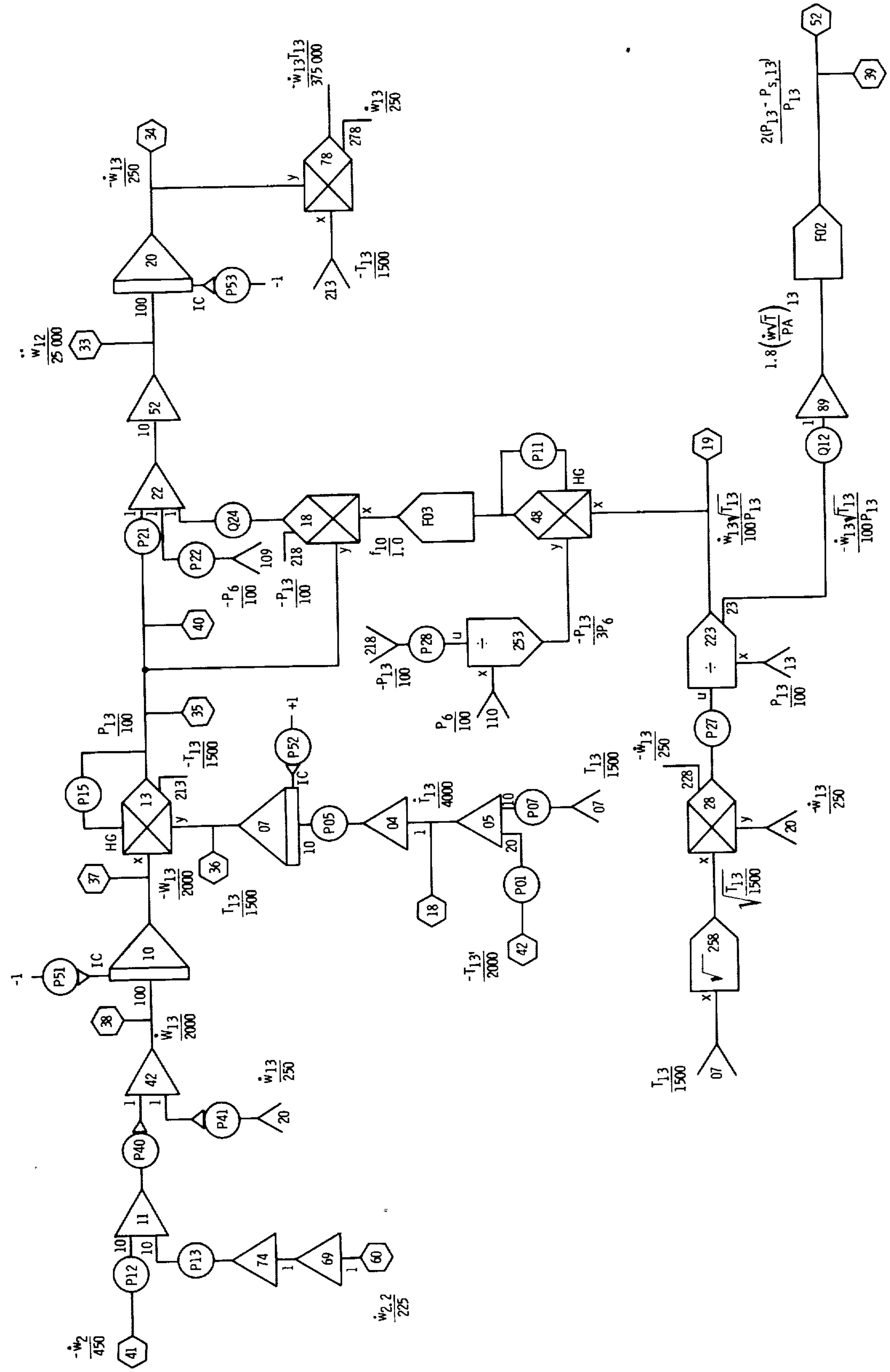

Fan duct - console 2

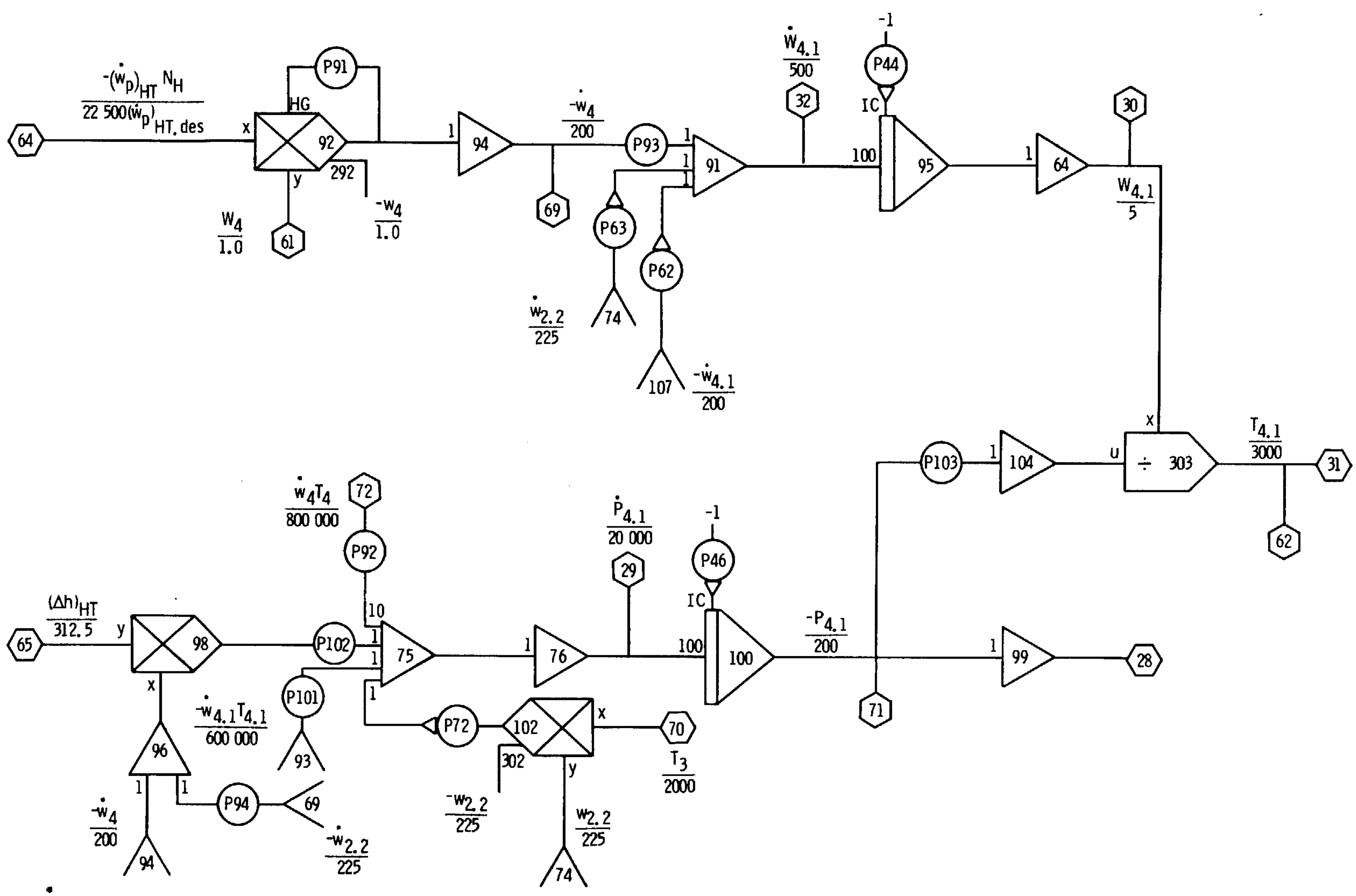

High pressure turbine and inter-turbine volume - console 2

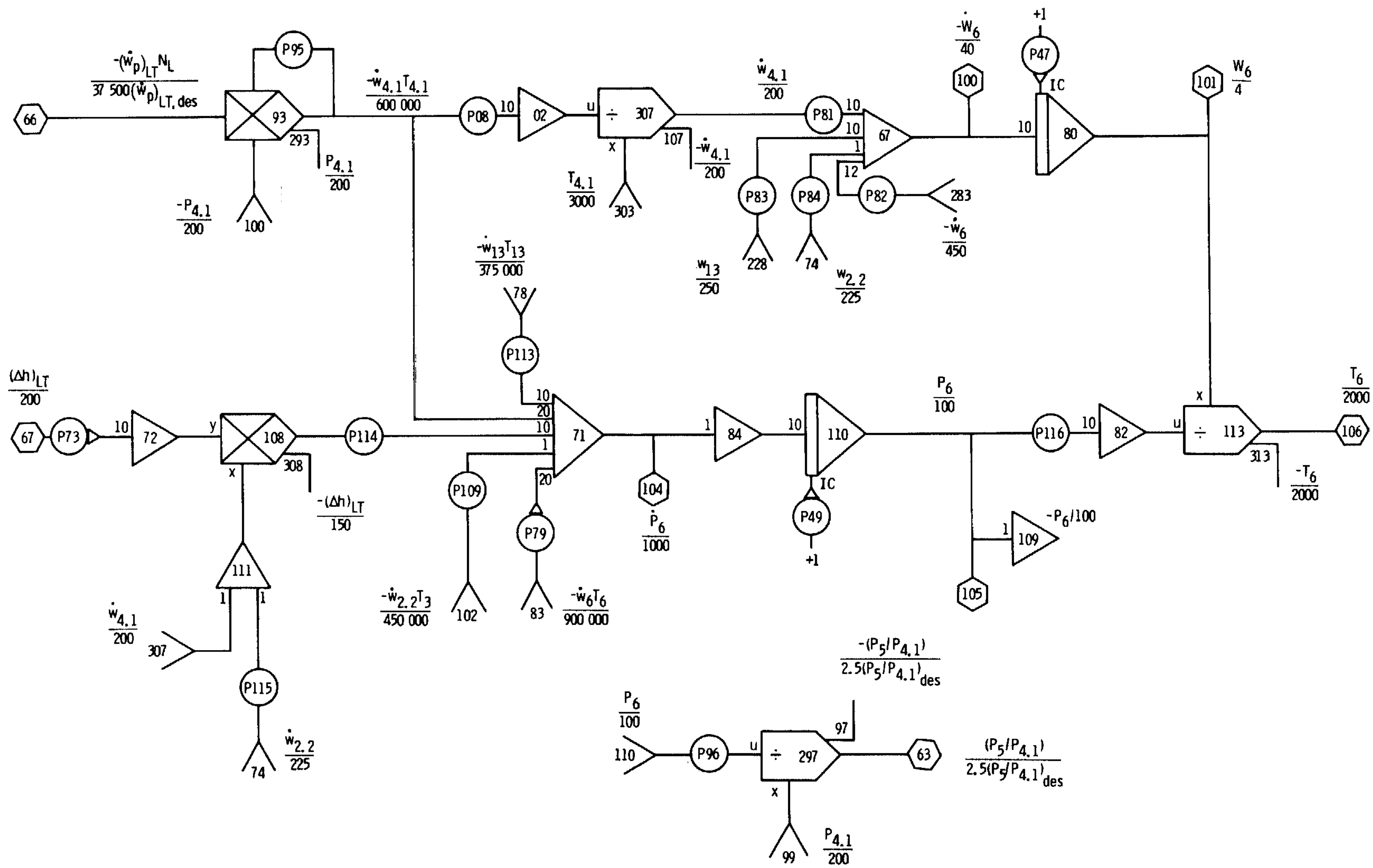

Low pressure turbine and mixing volume - console 2

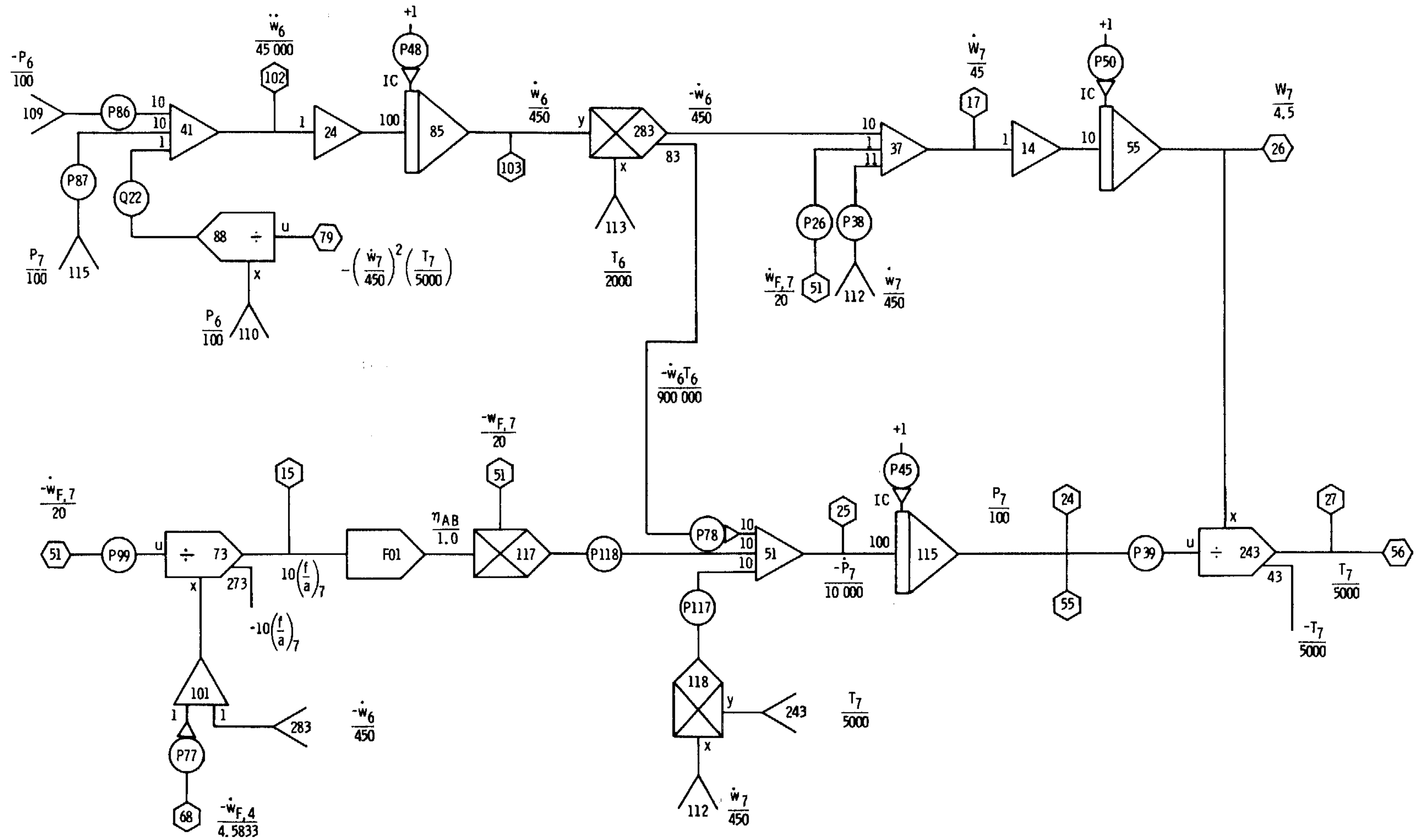

Augmentor - console 2

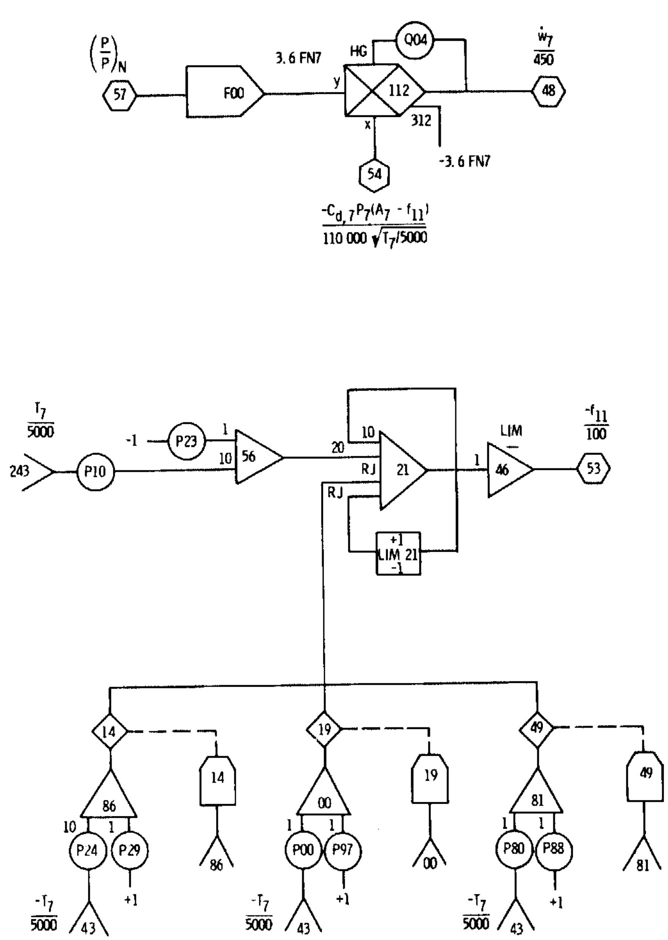

Nozzle - console 2

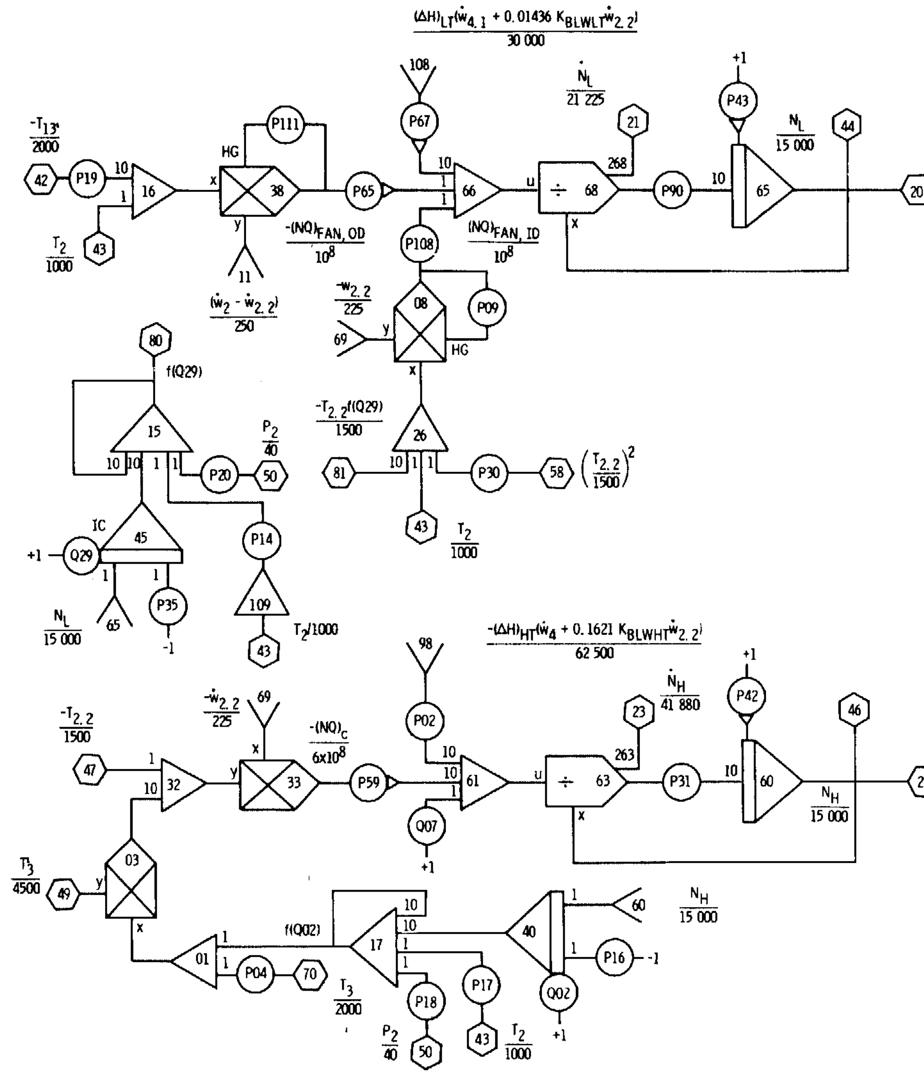

Torque balance - console 2

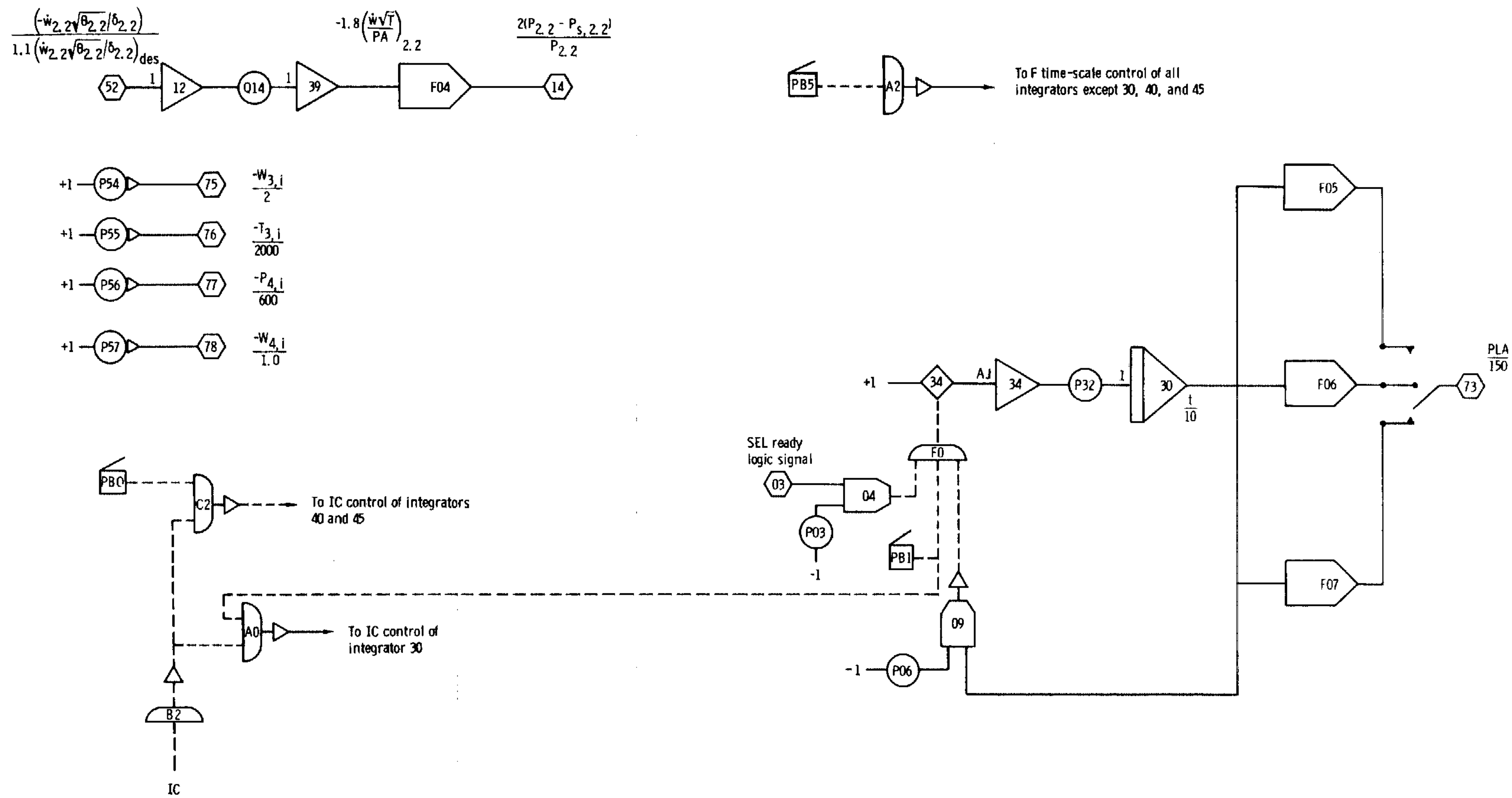

Miscellaneous - console 2

REFERENCES

1. Stone, C. R.; Miller, N. E.; Ward, M. D.; and Schmidt, R. D.: Turbine Engine Control Synthesis. Vol. I: Optimal Controller Synthesis and Demonstration Final Technical Report. AFAPL-TR-75-14-VOL-1, Honeywell, Inc. (AD-A014229), 1975.
2. Michael, Gerald J.; and Farrar, Florence A.: An Analytical Method for Synthesis of Nonlinear Multivariable Feedback Control. UARL-M941338-2, United Aircraft Corp. (AD-762797), 1973.
3. Michael, Gerald J.; and Farrar, Florence A.: Development of Optimal Control Modes for Advanced Technology Propulsion Systems. UARL-M911620-1, United Aircraft Corp. (AD-767425), 1974.
4. Bowles, Robert J.: Sub-Optimal Control of a Gas Turbine Engine. GE/EE/73A-1, Air Force Inst. Tech. (AD-777852), 1973.
5. Bentz, C. E.; and Zeller, J. R.: Integrated Propulsion Control System Program. SAE Paper 730359, April 1973.
6. Szuch, John R.; and Bruton, William M.: Real-Time Simulation of the TF30-P-3 Turbofan Engine Using A Hybrid Computer. NASA TM X-3106, 1974.
7. Szuch, John R.; and Seldner, Kurt: Real-Time Simulation of F100-PW-100 Turbofan Engine Using the Hybrid Computer. NASA TM X-3261, 1975.
8. Integrated Propulsion Control System (IPCS). Volume II - Technical Description. Boeing Aerospace Co. (AFAPL-TR-76-61), 1976.
9. Cwynar, David S.; and Batterton, Peter G.: Digital Implementation of the TF30-P-3 Turbofan Engine Control. NASA TM X-3105, 1974.
10. Deiters, R. M.; and Nomura, T.: Circle Test Evaluation of Method of Compensating Hybrid Computing Error by Predicted Integral. Simulation, vol. 8, no. 1, Jan. 1967, pp. 33-40.
11. Bekey, George A.; and Karplus, Walter J.: Hybrid Computation. John Wiley & Sons, Inc., 1968, pp. 117-124.
12. Szuch, John R.: Application of Real-Time Engine Simulations to the Development of Propulsion System Controls. NASA TM X-71764, 1975.

TABLE I. - DESIGN PARAMETERS

Compressor discharge volume, V_3, m^3	0.0468
Main-combustor volume, V_4, m^3	0.0468
Interturbine volume, $V_{4.1}$, m^3	0.6561
Mixing volume, V_6, m^3	0.8470
Augmentor volume, V_7, m^3	0.7128
Duct volume, V_{13}, m^3	1.427
Augmentor inductance, $(l/Ag_c)_{AB}$, $N\text{-}sec^2/kg\text{-}cm^2$	0.0007598
Duct inductance, $(l/Ag_c)_D$, $N\text{-}sec^2/kg\text{-}cm^2$	0.0007598
High-speed rotor inertia, I_H, $N\text{-}cm\text{-}sec^2$	565.35
Low-speed rotor inertia, I_L, $N\text{-}cm\text{-}sec^2$	610.00
Main-combustor pressure loss coefficient, K_B, $N^2 sec^2/cm^4\text{-}K\text{-}kg^2$	0.00114
Low-pressure-turbine discharge pressure loss coefficient, K_{PR5}	1.024
Augmentor pressure loss coefficient, K_{AB}, $N^2\text{-}sec^2/cm^4\text{-}K\text{-}kg^2$	3.5659×10^{-6}
Nozzle flow coefficient, K_N, $kg\text{-}K^{1/2}/N\text{-}sec$	0.1509
Fraction of high-pressure-turbine cooling bleed that performs work, K_{BLWHT}	0.6292
Fraction of low-pressure-turbine cooling bleed that performs work, K_{BLWLT}	0.1114
Fan inlet specific heat, $c_{p,2}$, J/kg-K	1009
Compressor inlet specific heat, $c_{p,2.2}$, J/kg-K	1001
Compressor discharge specific heat, $c_{p,3}$, J/kg-K	1039
Main-combustor specific heat, $c_{p,4}$, J/kg-K	1145
Interturbine specific heat, $c_{p,4.1}$, J/kg-K	1116
Mixing-volume specific heat, $c_{p,6}$, J/kg-K	1062
Augmentor specific heat, $c_{p,7}$, J/kg-K	1062
Duct inlet specific heat, $c_{p,13'}$, J/kg-K	1009
Duct discharge specific heat, $c_{p,16}$, J/kg-K	1030
Main-combustor specific heat ratio, γ_4	[a]1.292
Interturbine specific heat ratio, $\gamma_{4.1}$	1.306
Mixing volume specific heat ratio, γ_6	1.344
Augmentor specific heat ratio, γ_7	[b]1.359
Compressor discharge temperature time constant, τ_3, sec	0.05
Duct temperature time constant, τ_{13}, sec	0.05
Heating value, HVF, J/kg	4.407×10^7

[a]Effectively decreased by a factor of 20 to match baseline digital data.
[b]Effectively decreased by a factor of 10 to increase simulation stability.

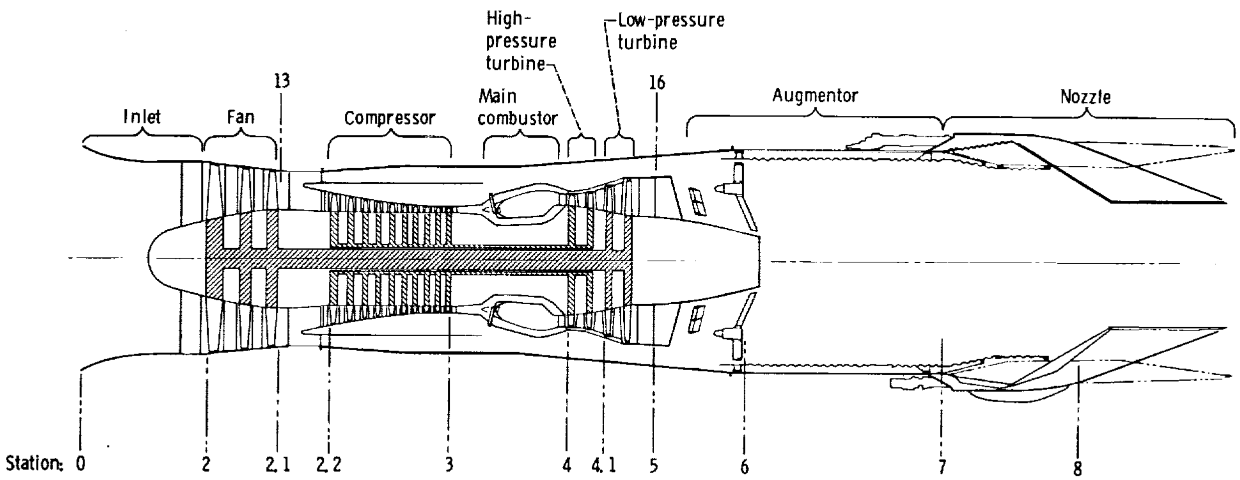

Figure 1. - Schematic representation of F100-PW-100(3) augmented turbofan engine.

CD-11819-07

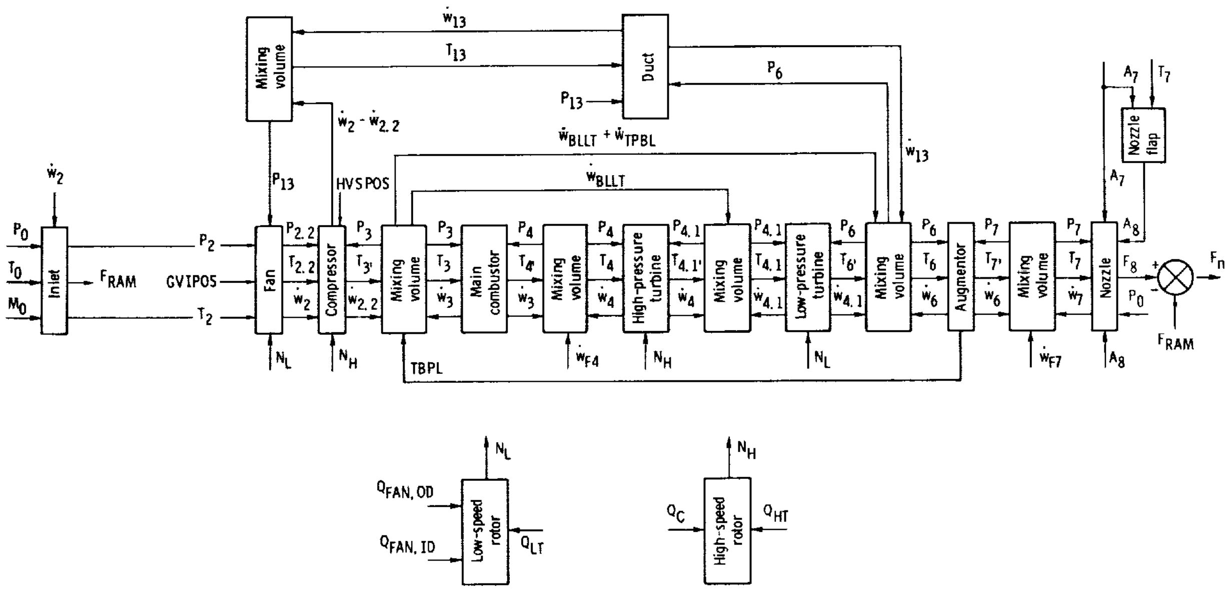

Figure 2. - Computational flow diagram of real-time F100-PW-100(3) engine simulation.

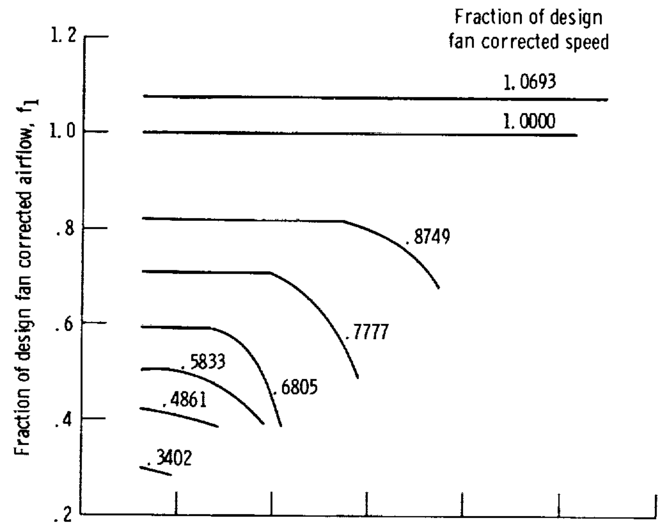

(a) Fan tip.

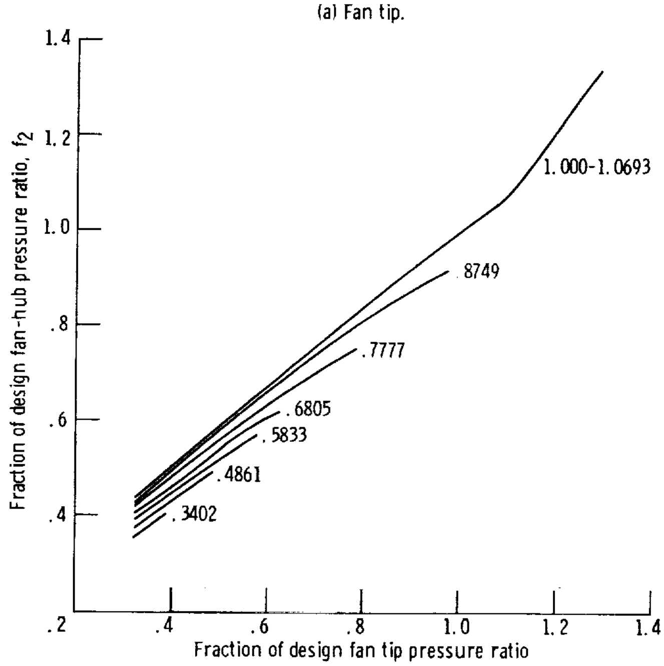

(b) Fan hub.

Figure 3. - F100-PW-100(3) fan performance maps with inlet guide vanes at their nominally scheduled position. No Reynolds number effects.

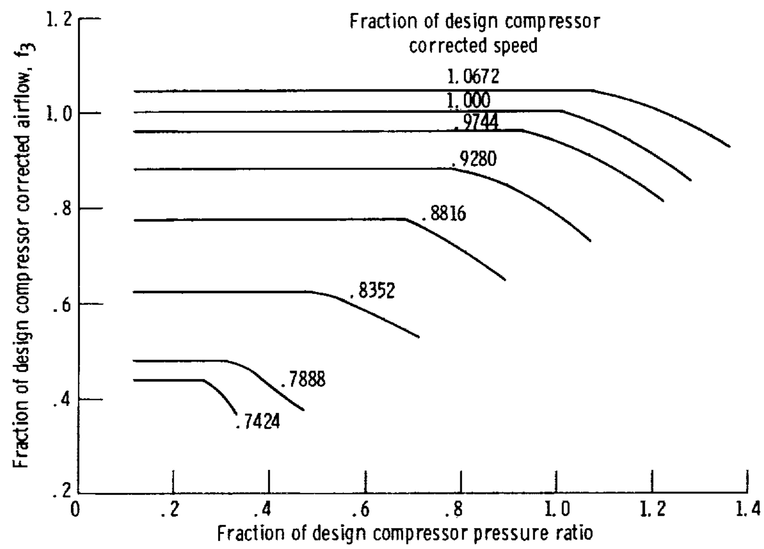

Figure 5. - F100-PW-100(3) compressor performance map with stator vanes at their nominally scheduled position.

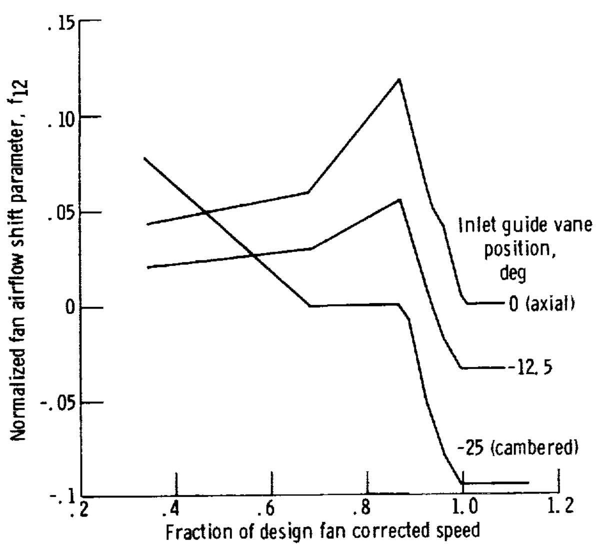

Figure 4. - Effect of variable inlet guide vane position on F100-PW-100(3) fan performance map.

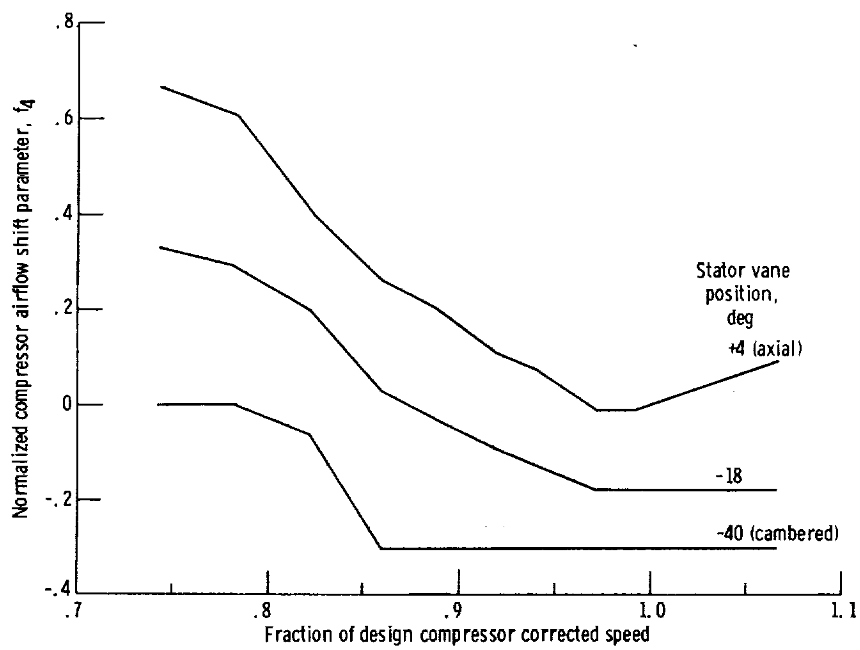

Figure 6. - Effect of variable stator vane position on F-100-PW-100(3) compressor performance map.

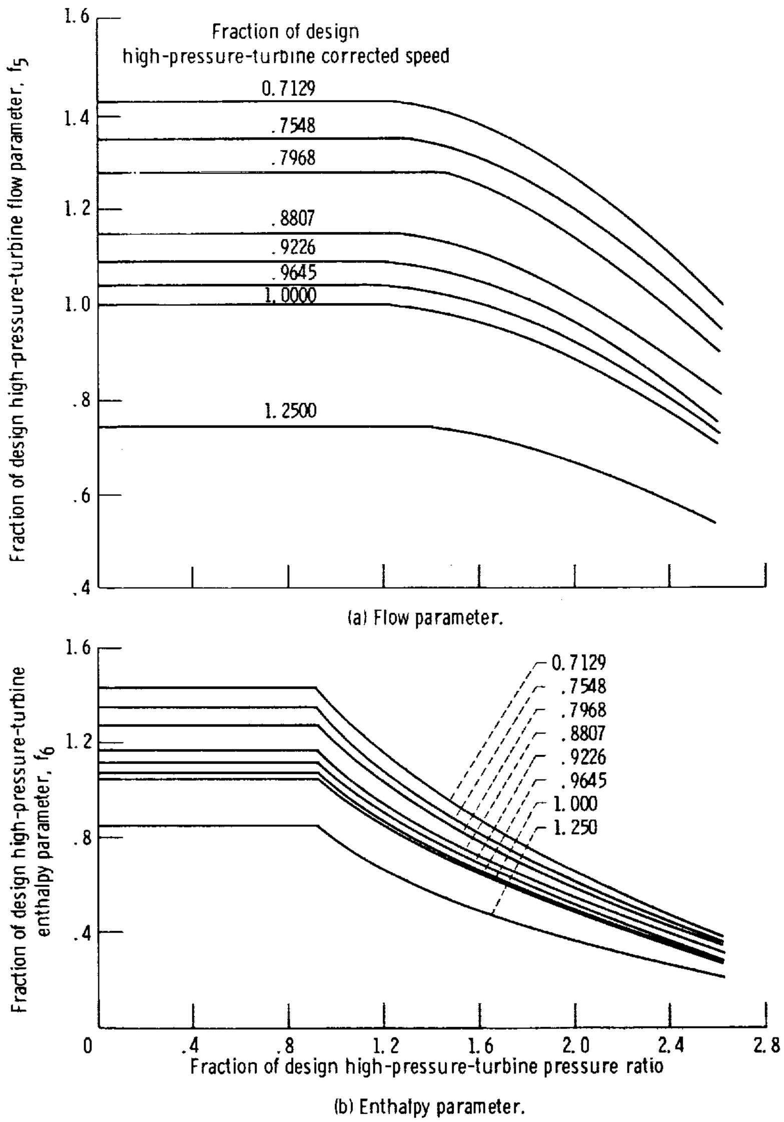

Figure 7. - F100-PW-100(3) high-pressure-turbine performance maps.

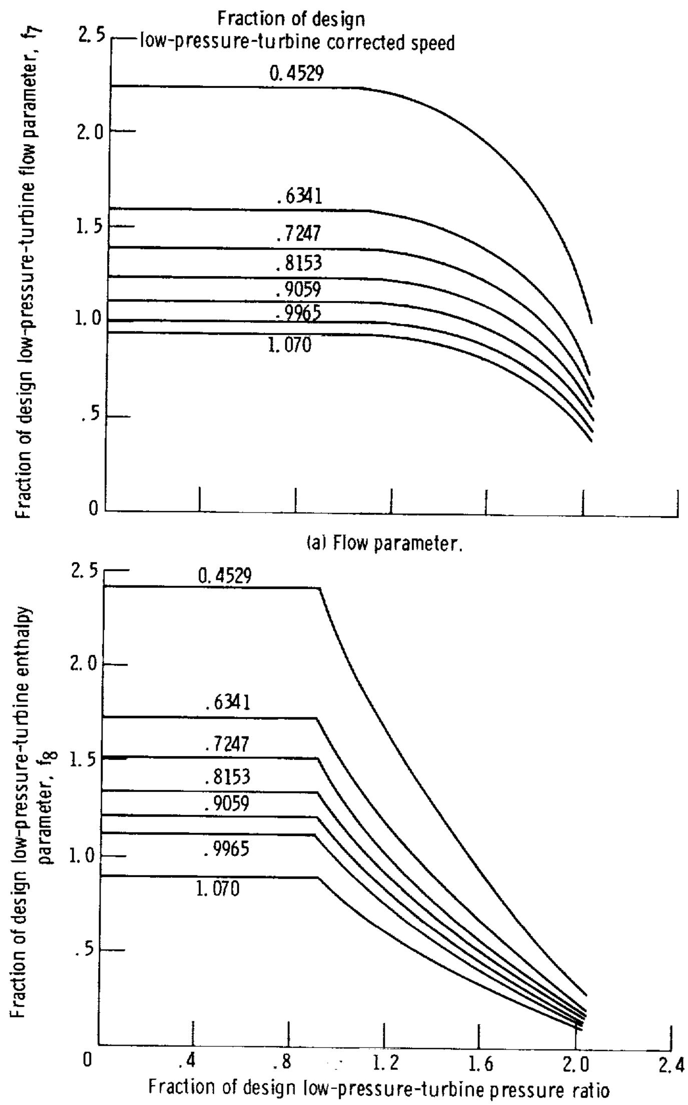

(b) Enthalpy parameter.

Figure 8. - F100-PW-100(3) low-pressure-turbine performance maps.

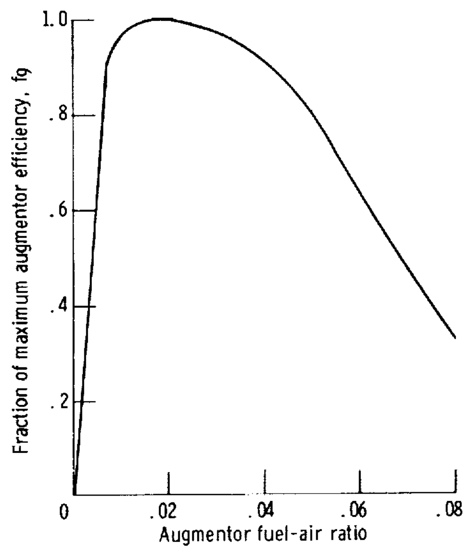

Figure 9. - F100-PW-100(3) augmentor efficiency function.

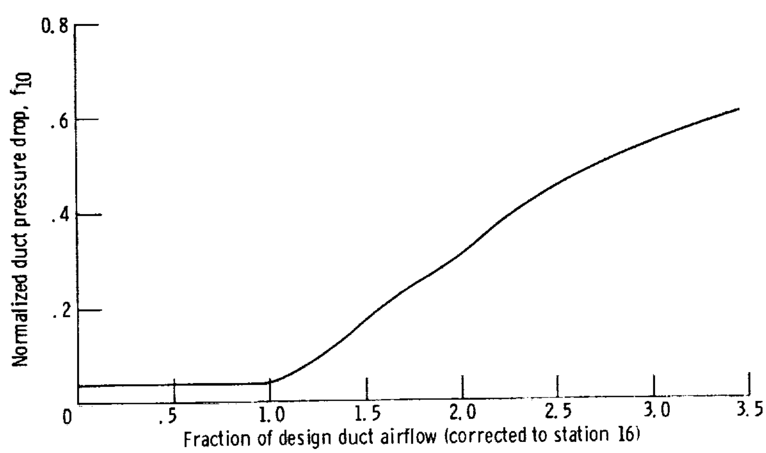

Figure 10. - F100-PW-100(3) duct pressure loss function.

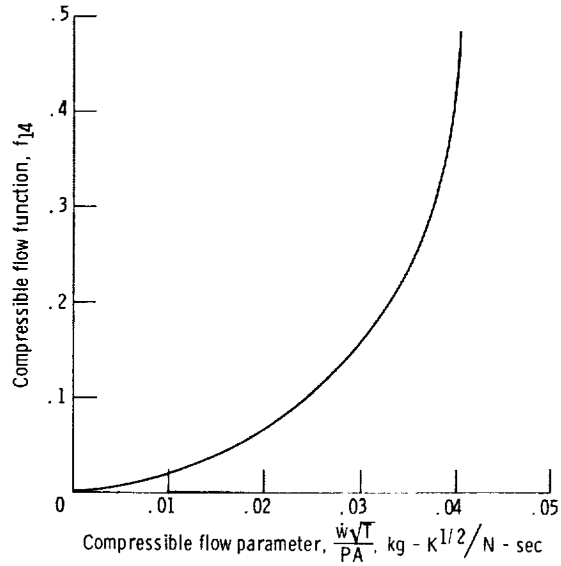

Figure 11. - Compressible flow function.

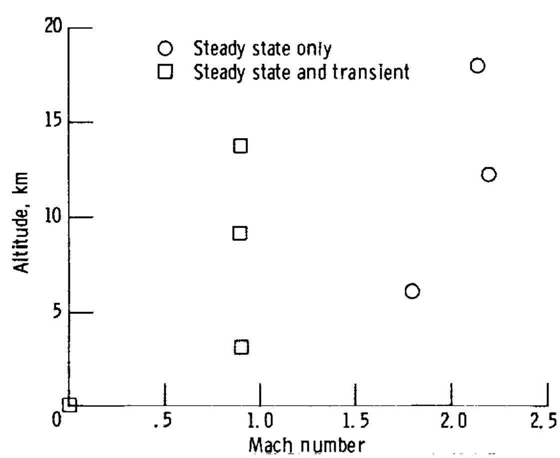

Figure 12. - F100-PW-100(3) hybrid simulation evaluation points.

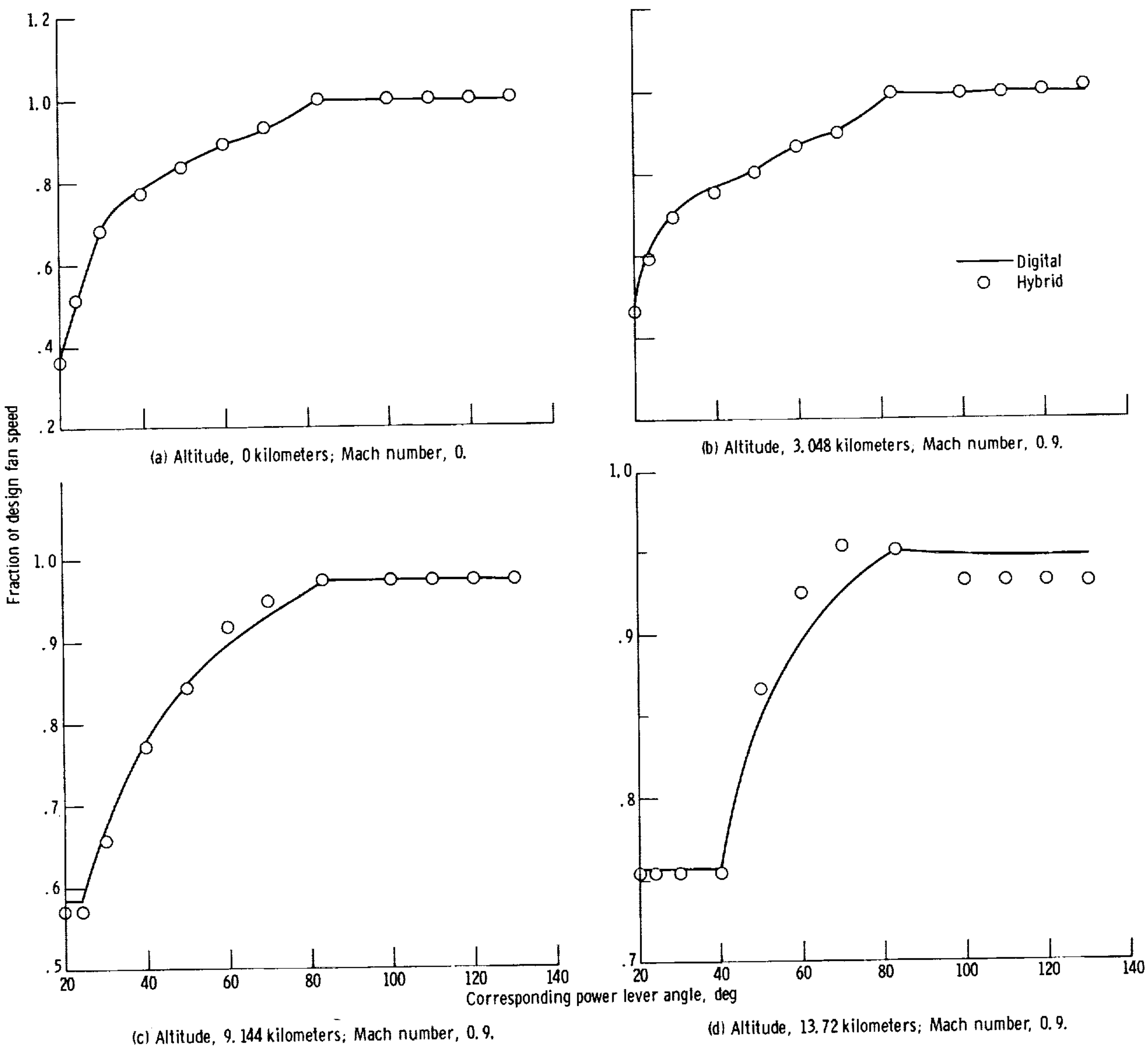

Figure 13. - Comparison of open-loop hybrid and baseline digital steady-state data for fan speed at standard-day conditions.

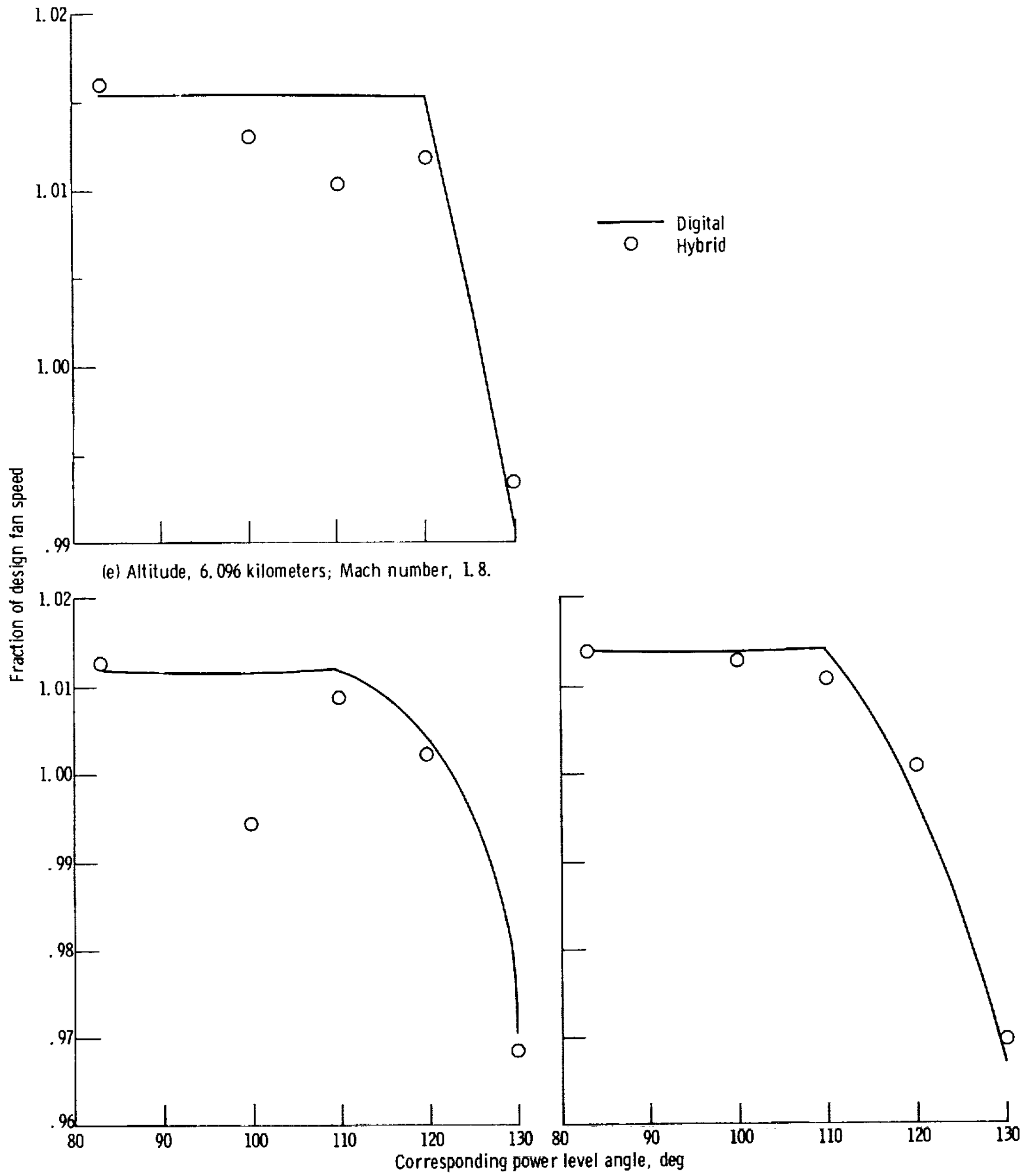

(e) Altitude, 6.096 kilometers; Mach number, 1.8.

(f) Altitude, 12.19 kilometers; Mach number, 2.2.

(g) Altitude, 17.83 kilometers; Mach number, 2.15.

Figure 13. - Concluded.

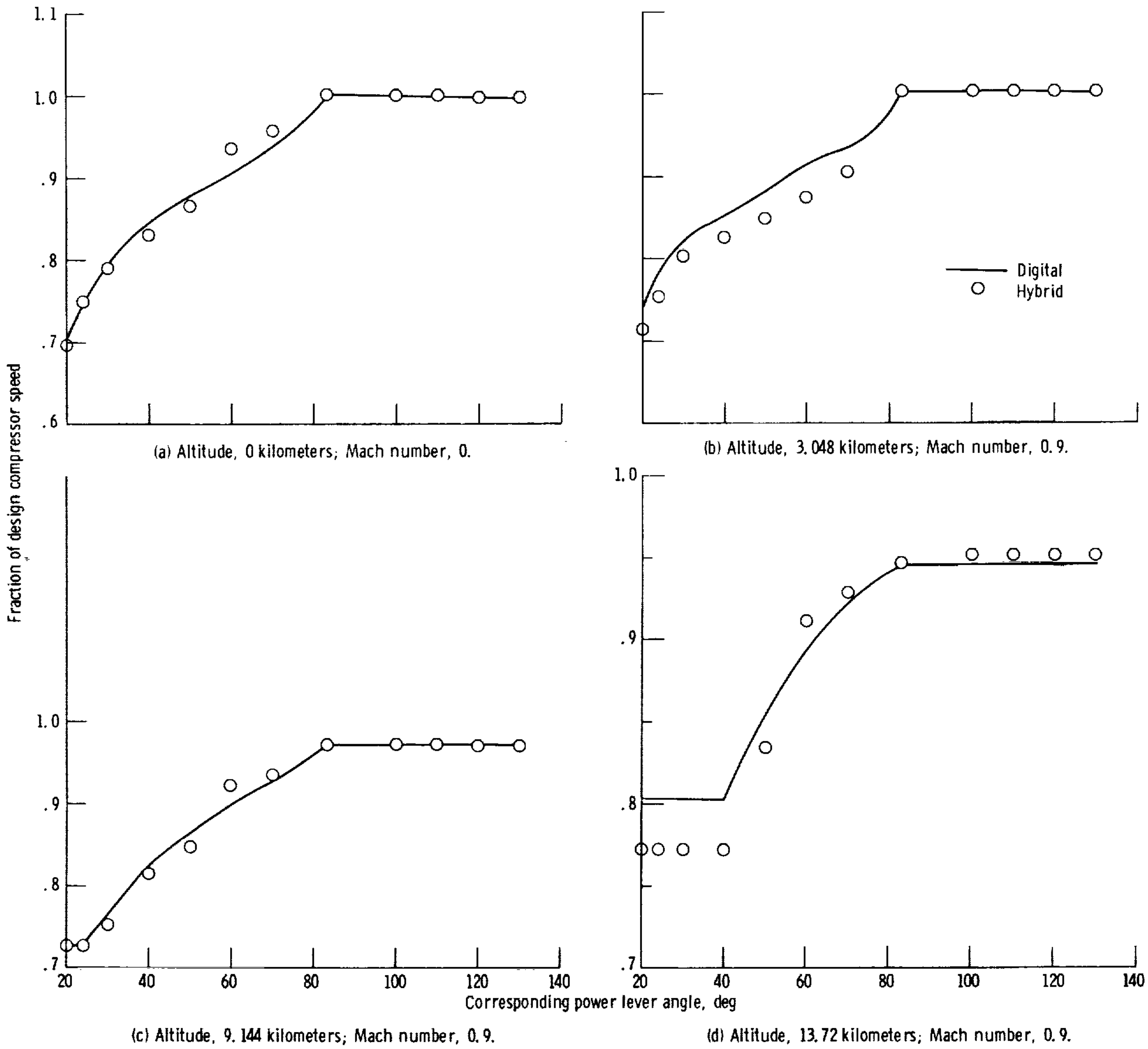

Figure 14. - Comparison of open-loop hybrid and baseline digital steady-state data for compressor speed at standard-day conditions.

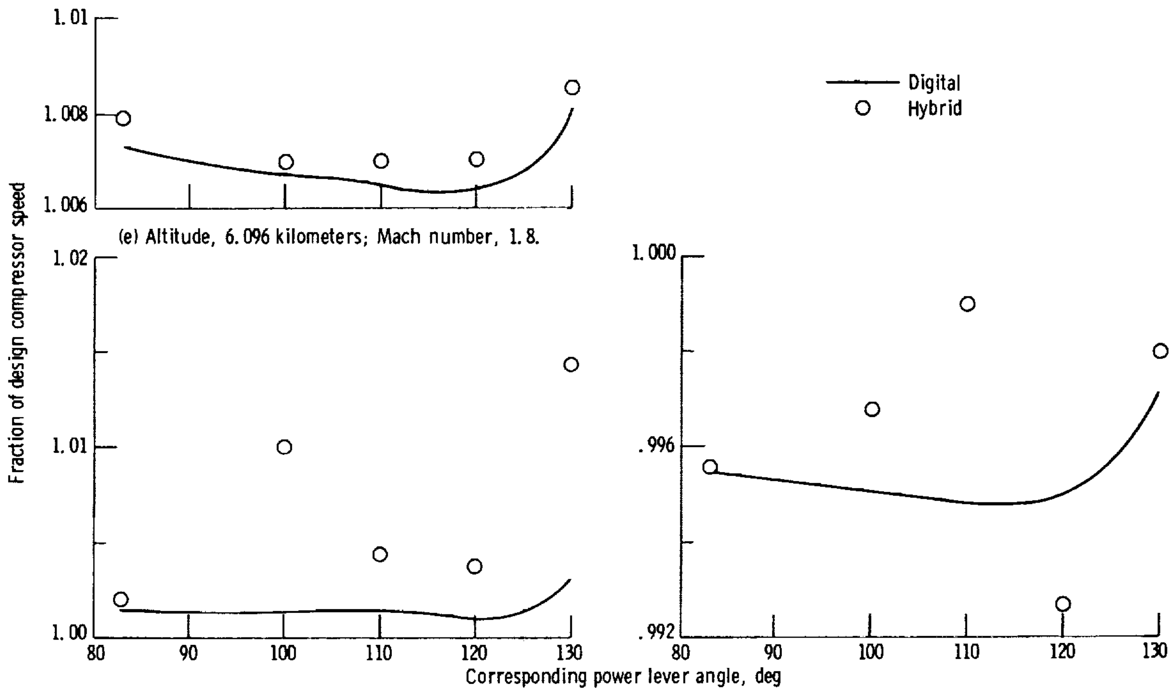

(e) Altitude, 6.096 kilometers; Mach number, 1.8.

(f) Altitude, 12.19 kilometers; Mach number, 2.2.

(g) Altitude, 17.83 kilometers; Mach number, 2.15.

Figure 14. - Concluded.

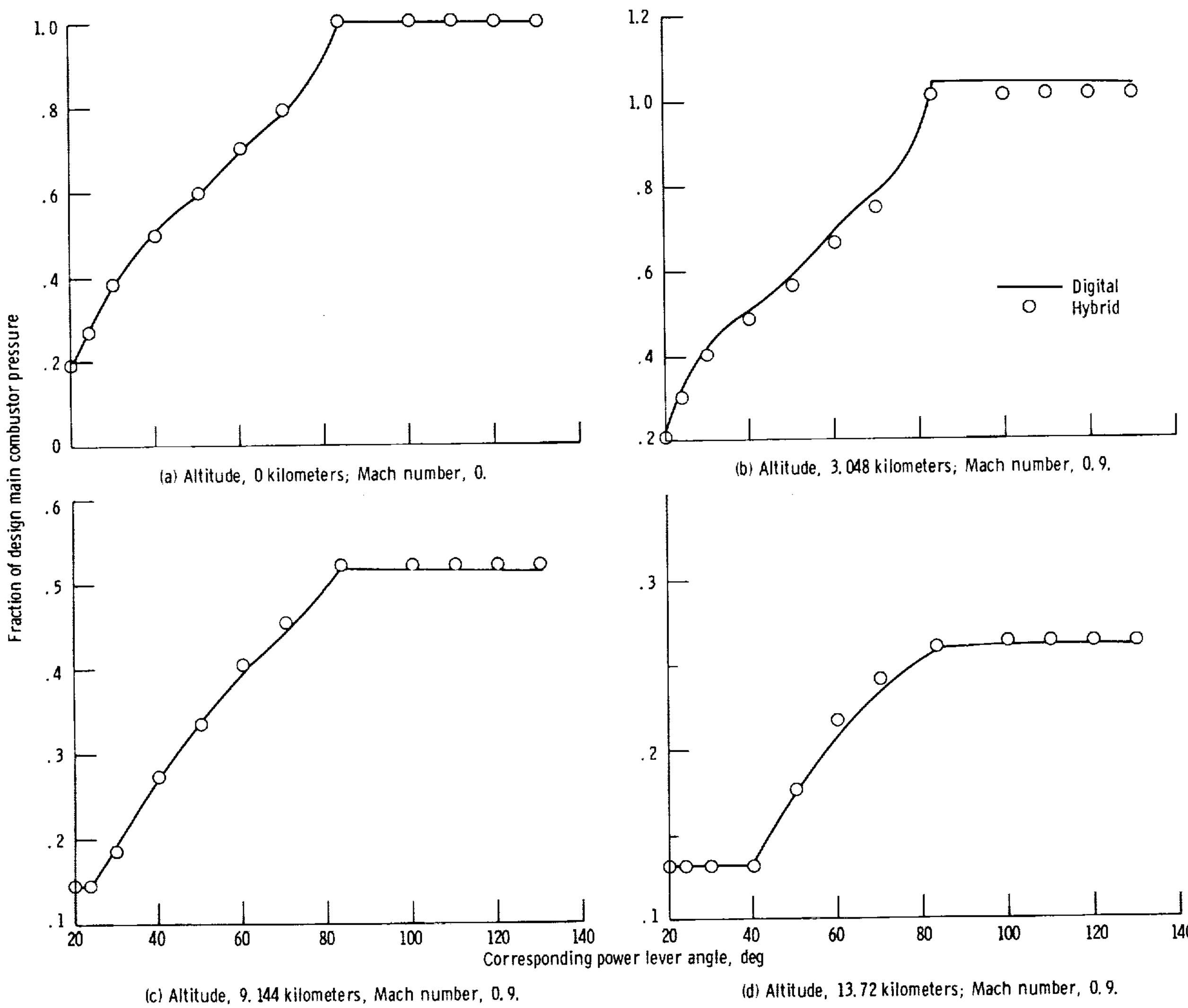

Figure 15. - Comparison of open-loop hybrid and baseline digital steady-state data for main combustor pressure at standard-day conditions.

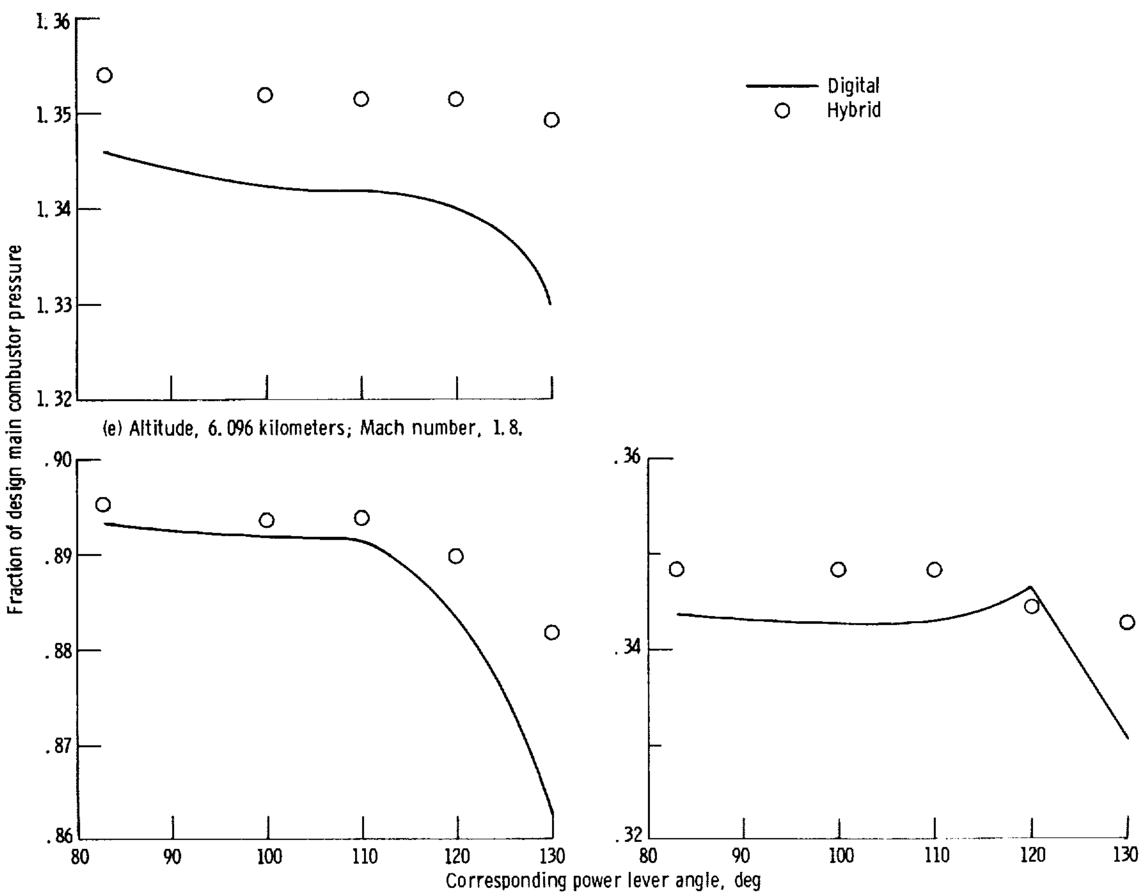

(f) Altitude, 12.19 kilometers; Mach number, 2.2.

(g) Altitude, 17.83 kilometers; Mach number, 2.15.

Figure 15. - Concluded.

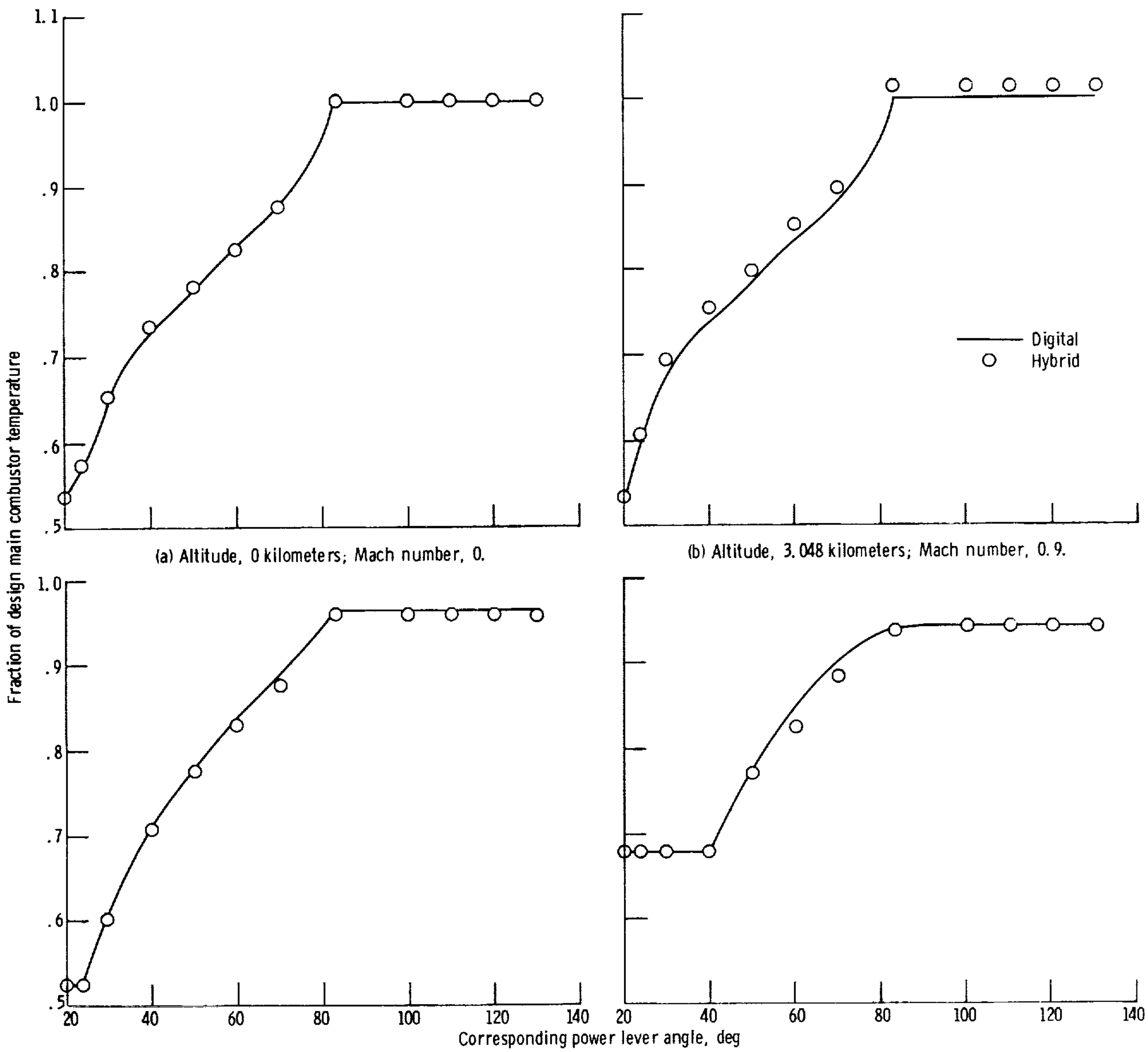

Figure 16. - Comparison of open-loop hybrid and baseline digital steady-state data for main combustor temperature at standard-day conditions.

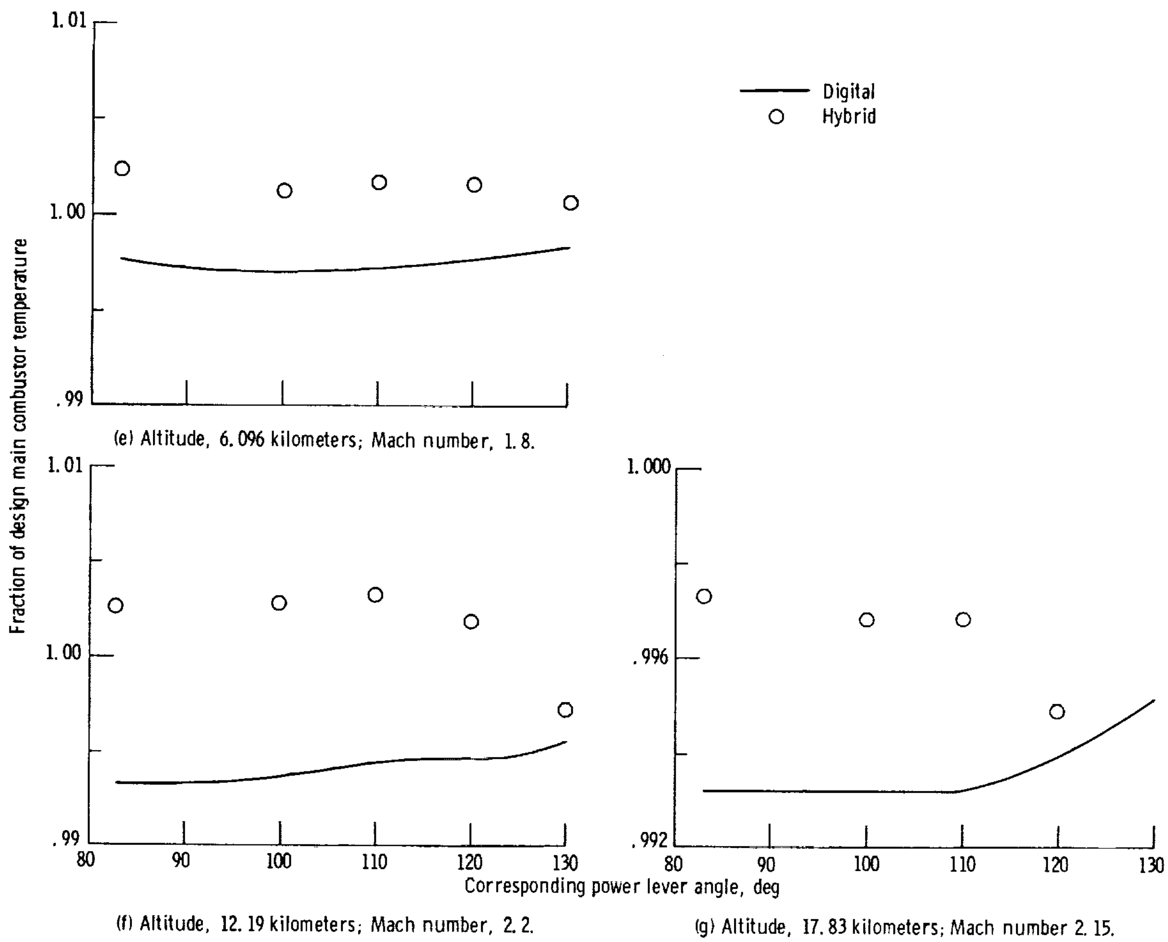

Figure 16. - Concluded.

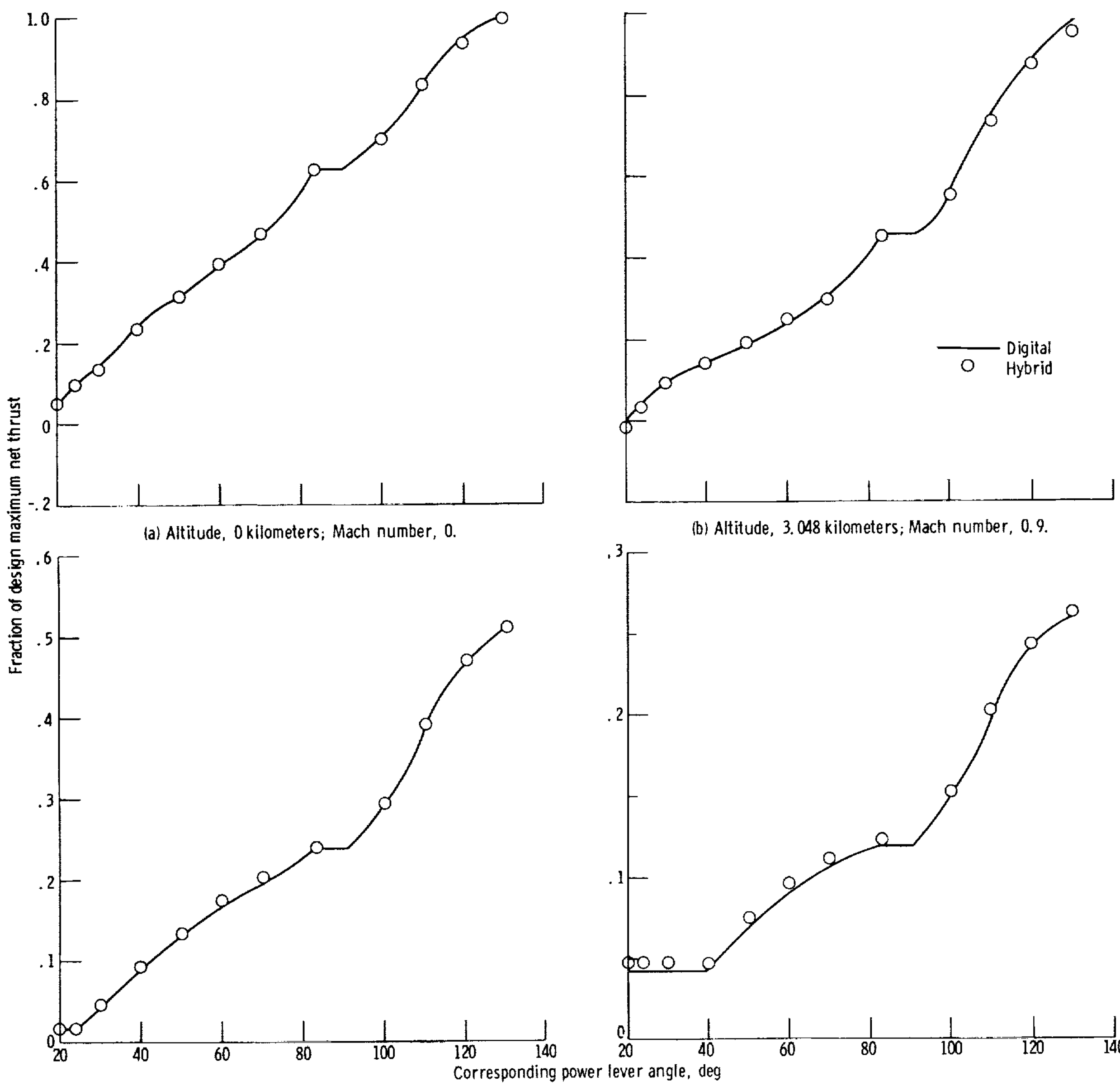

Figure 17. - Comparison of open-loop hybrid and baseline digital steady-state data for net thrust at standard-day conditions.

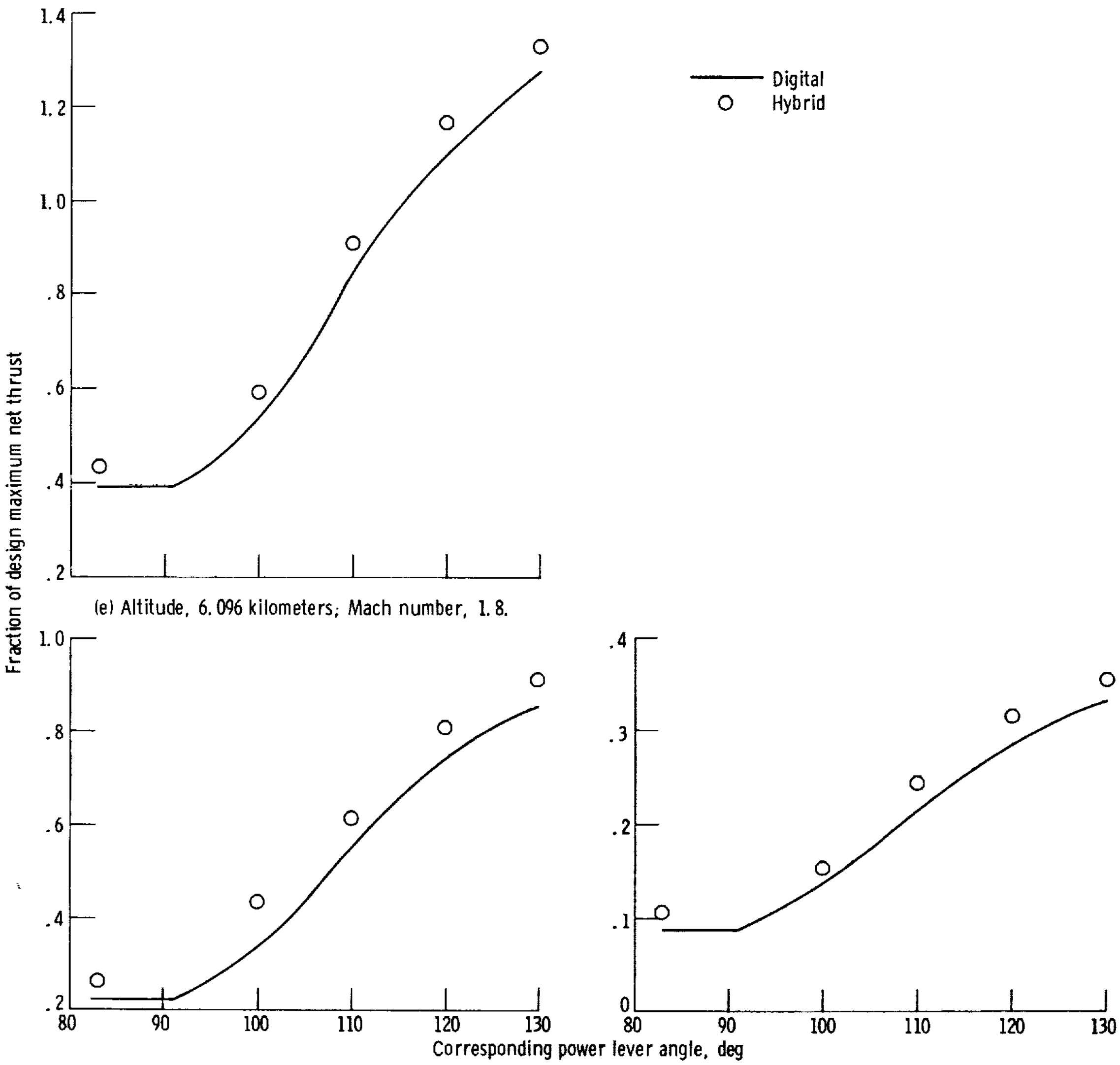

(f) Altitude, 12.19 kilometers; Mach number, 2.2.

(g) Altitude, 17.83 kilometers; Mach number, 2.15.

Figure 17. - Concluded.

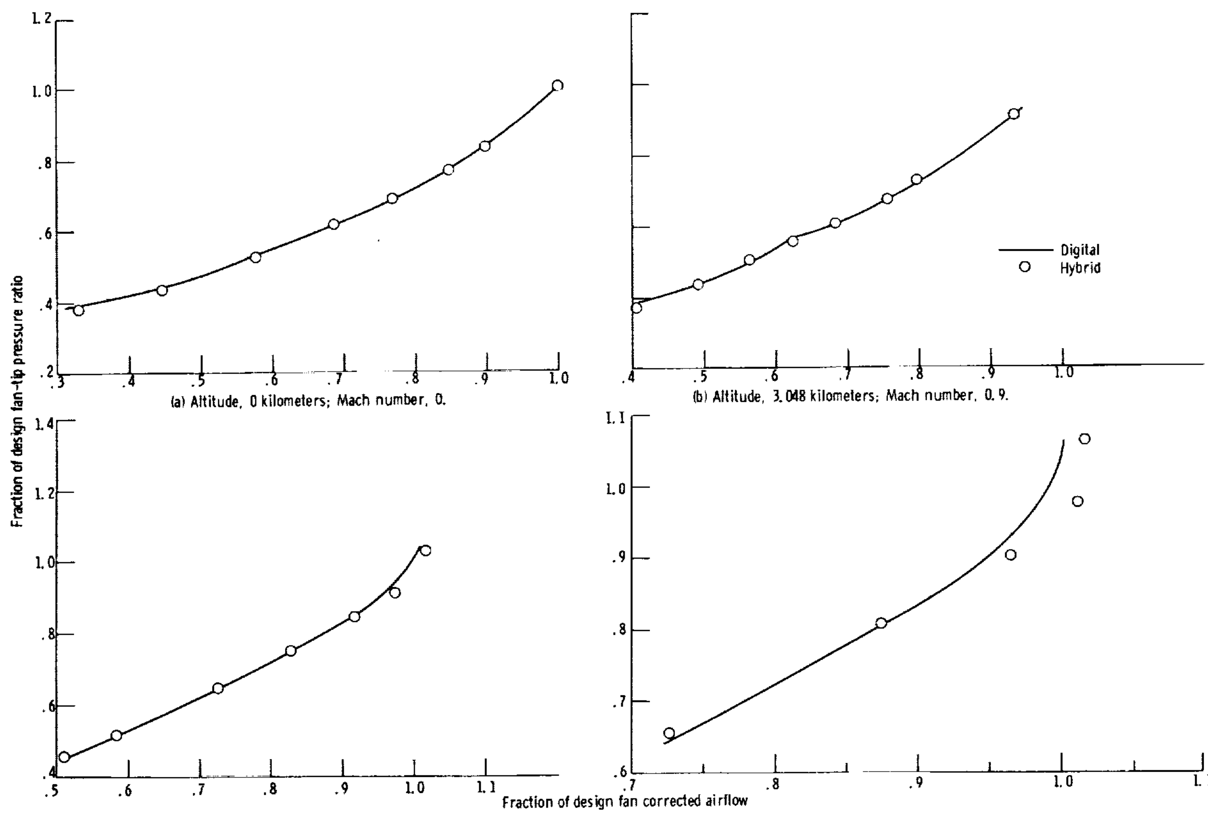

(a) Altitude, 0 kilometers; Mach number, 0.

(b) Altitude, 3.048 kilometers; Mach number, 0.9.

(c) Altitude, 9.144 kilometers; Mach number, 0.9.

(d) Altitude, 13.72 kilometers; Mach number, 0.9.

Figure 18. - Comparison of open-loop hybrid and baseline digital steady-state data for fan operating line at standard-day conditions.

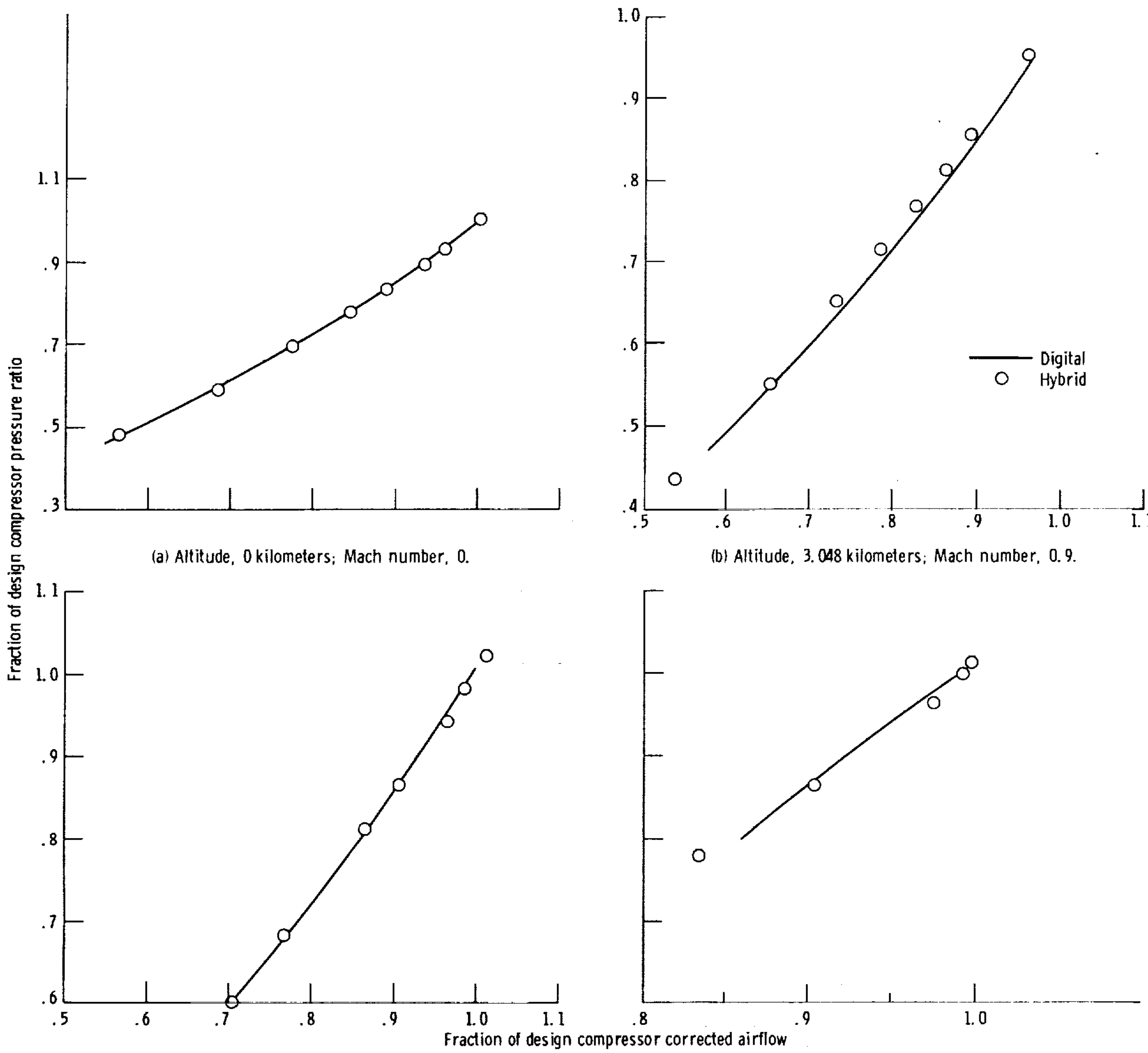

Figure 19. - Comparison of open-loop hybrid and baseline digital steady-state data for compressor operating line at standard-day conditions.

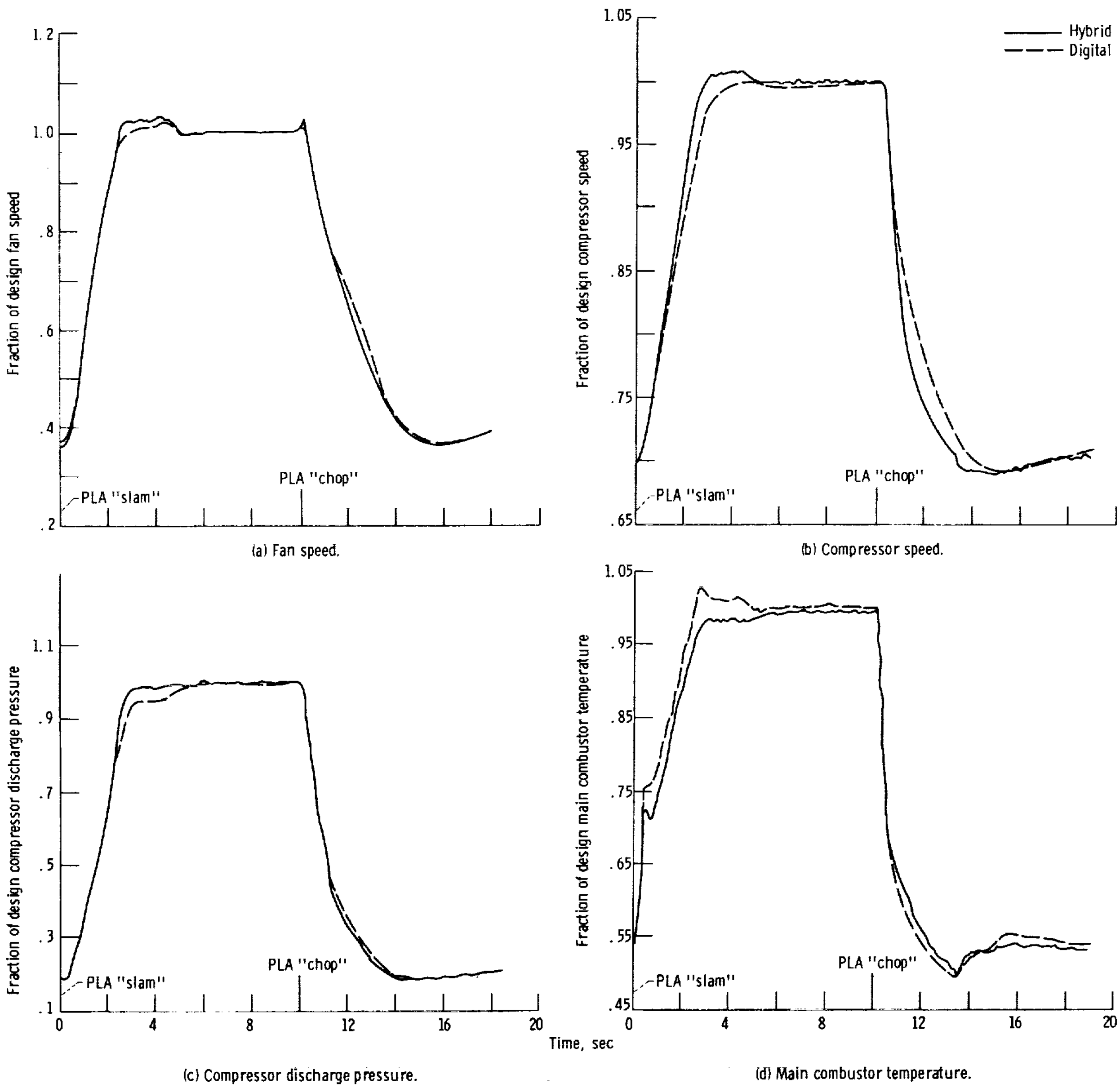

Figure 20. - Comparison of scheduled-input hybrid and baseline digital transient data for idle to 83° to idle power lever movement. Altitude, 0 kilometers; Mach number, 0.

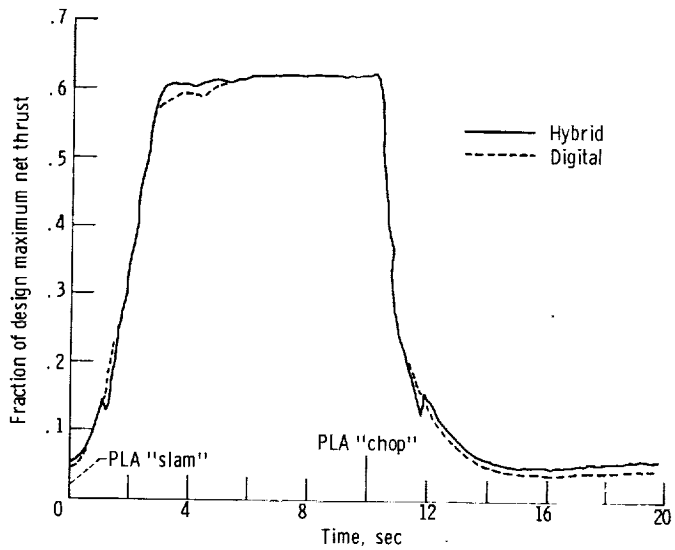

(e) Net thrust.

Figure 20. - Concluded.

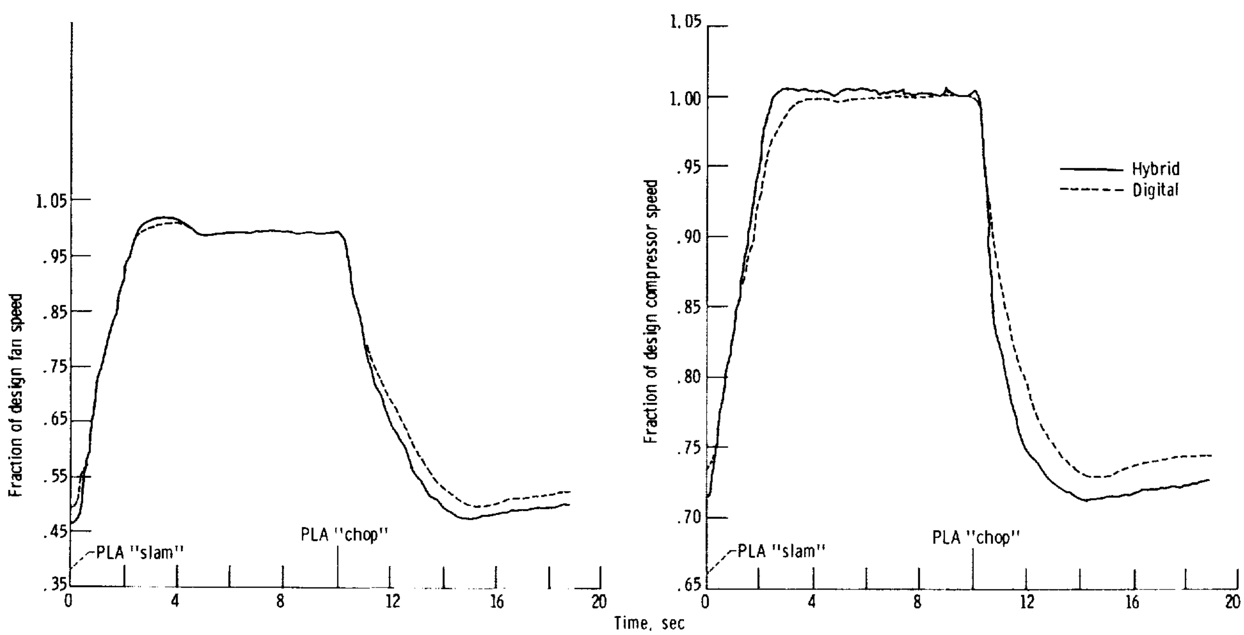

(a) Fan speed.

(b) Compressor speed.

Figure 21. - Comparison of scheduled-input hybrid and baseline digital transient data for idle to 83° to idle power lever movement. Altitude, 3.048 kilometers; Mach number, 0.9.

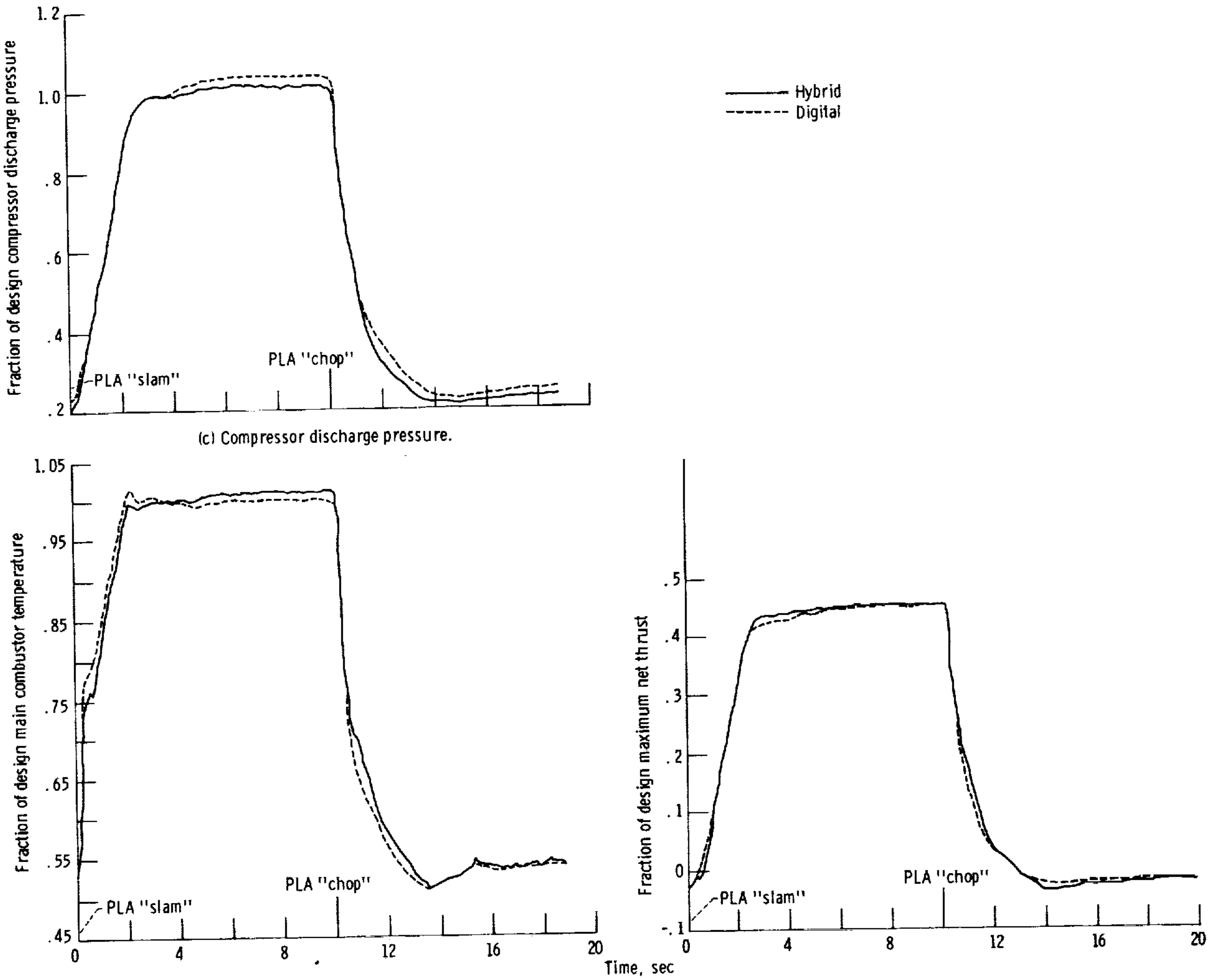

(c) Compressor discharge pressure.

(d) Main combustor temperature.

(e) Net thrust.

Figure 21. - Concluded.

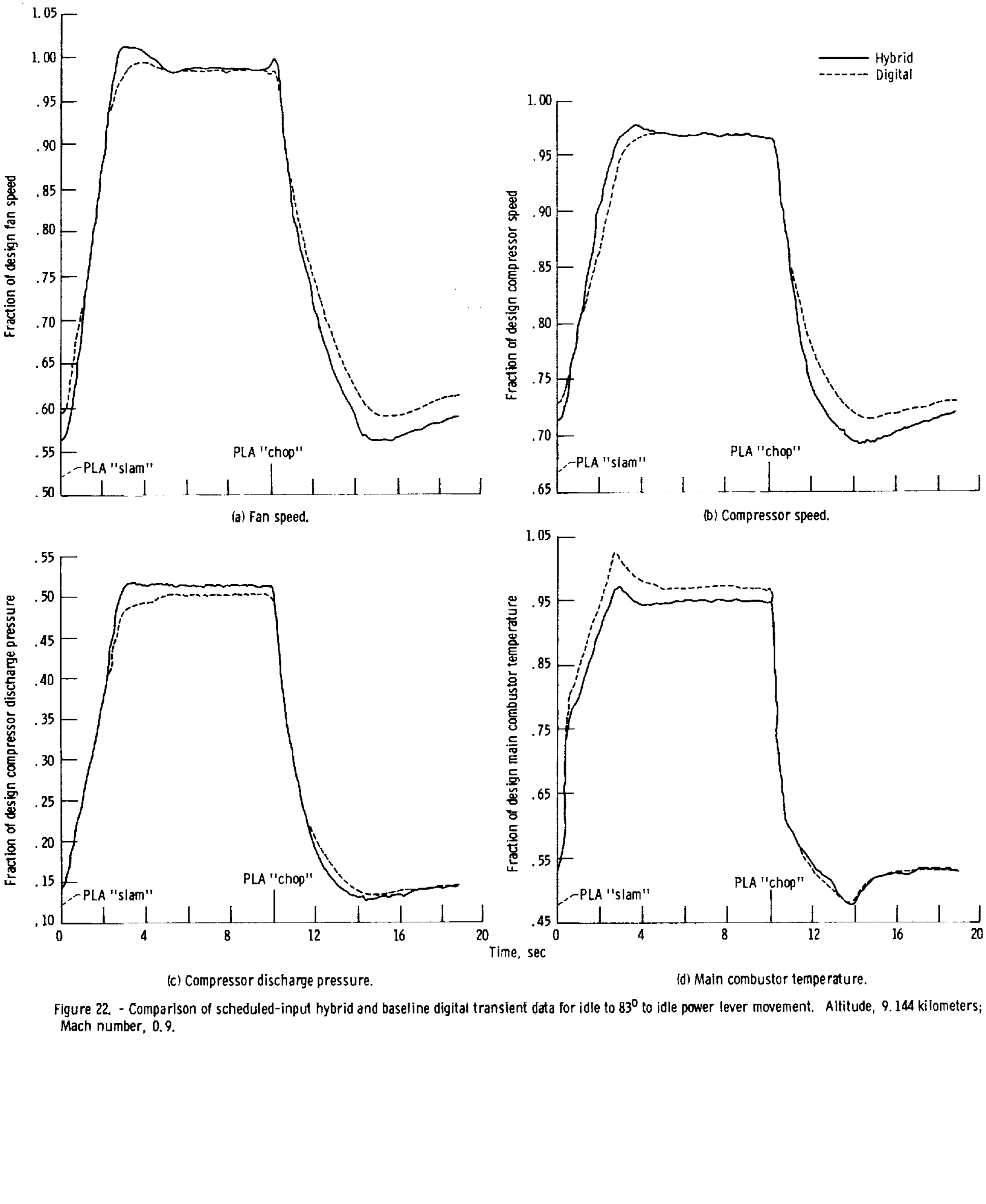

Figure 22. - Comparison of scheduled-input hybrid and baseline digital transient data for idle to 83° to idle power lever movement. Altitude, 9.144 kilometers; Mach number, 0.9.

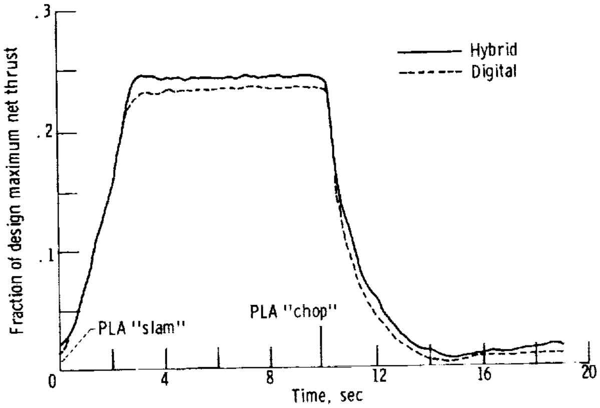

(e) Net thrust.

Figure 22. - Concluded.

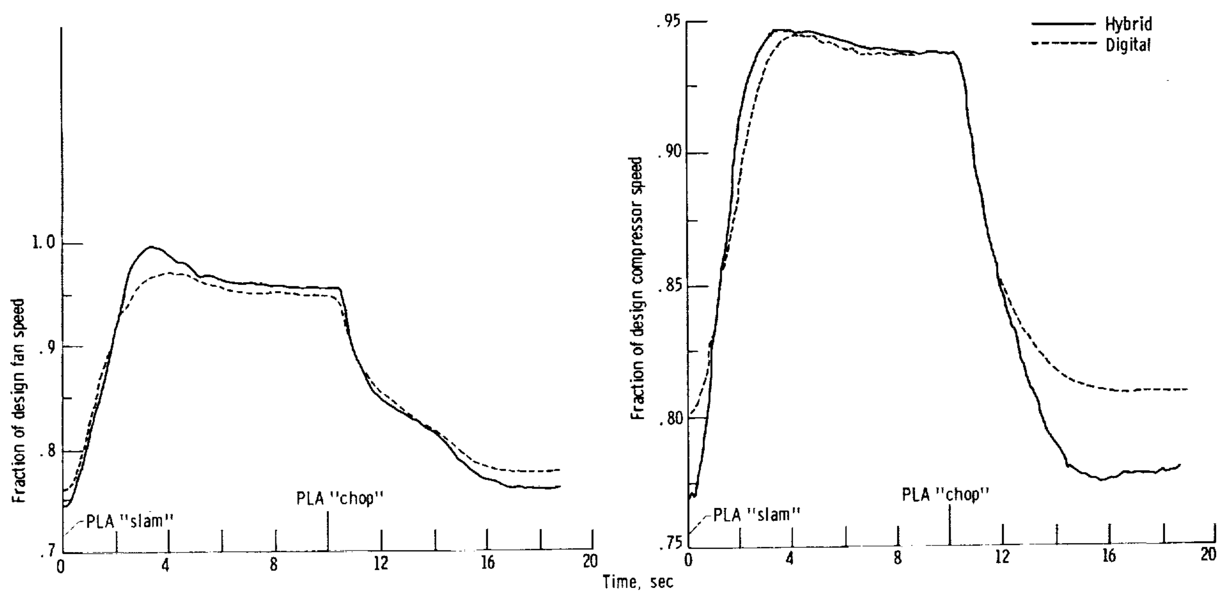

(a) Fan speed.

(b) Compressor speed.

Figure 23. - Comparison of scheduled-input hybrid and baseline digital transient data for idle to 83° to idle power lever movement. Altitude, 13.72 kilometers; Mach number, 0.9.

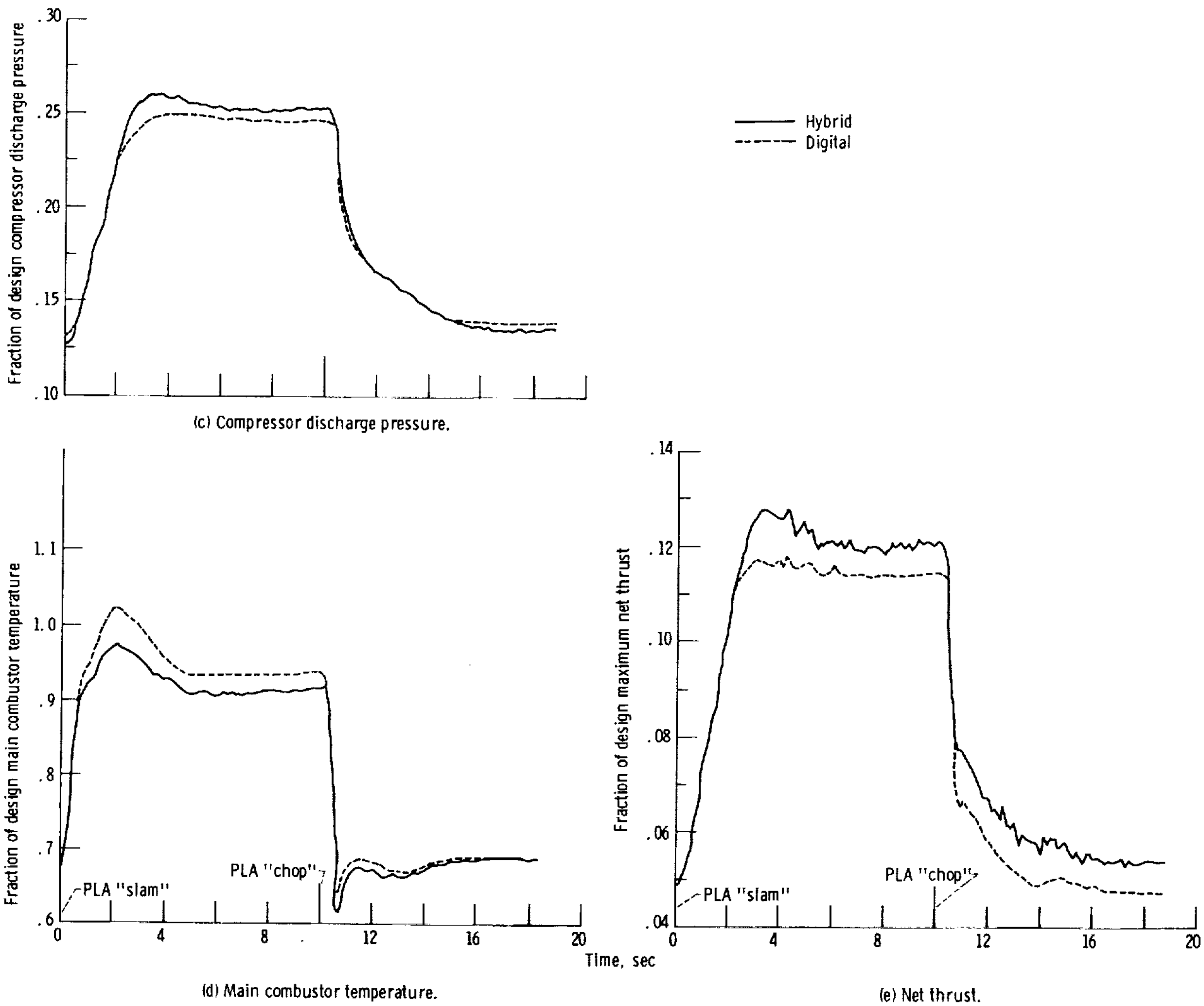

Figure 23. - Concluded.

1. Report No. NASA TP-1034	2. Government Accession No.	3. Recipient's Catalog No.
4. Title and Subtitle DEVELOPMENT AND VERIFICATION OF REAL-TIME, HYBRID COMPUTER SIMULATION OF F100-PW-100(3) TURBOFAN ENGINE		5. Report Date September 1977
		6. Performing Organization Code
7. Author(s) John R. Szuch, Kurt Seldner, and David S. Cwynar		8. Performing Organization Report No. E-9090
		10. Work Unit No. 505-05
9. Performing Organization Name and Address National Aeronautics and Space Administration Lewis Research Center Cleveland, Ohio 44135		11. Contract or Grant No.
		13. Type of Report and Period Covered Technical Paper
12. Sponsoring Agency Name and Address National Aeronautics and Space Administration Washington, D.C. 20546		14. Sponsoring Agency Code
15. Supplementary Notes		

16. Abstract

Real-time simulations can facilitate the development of digital controls for airbreathing propulsion systems. This report describes a real-time, hybrid computer simulation of the F100-PW-100(3) turbofan engine. The simulation is intended to support controls research programs involving that engine. Data are presented to show that the real-time simulation does match the predicted steady-state and transient performance of the engine over a wide range of flight conditions and power settings. This report includes the simulation equations, FORTRAN listings, and analog patching diagrams.

17. Key Words (Suggested by Author(s)) Simulation; Hybrid computer; Turbofan; Real time; Transient; Dynamics		18. Distribution Statement Unclassified - unlimited STAR Category 07	
19. Security Classif. (of this report) Unclassified	20. Security Classif. (of this page) Unclassified	21. No. of Pages 75	22. Price* A04

* For sale by the National Technical Information Service, Springfield, Virginia 22161

NASA-Langley, 1977